Analysing spiral eddies as an example of baroclinic Mixed Layer Instabilities

Master Thesis in Physical Oceanography

presented to the Department of Geosciences, University of Hamburg

supervised by Prof. Dr. Carsten Eden and Nils Brüggemann

Hannah Kleppin

November 6, 2012

Abstract

An asymmetry between anticyclonic and cyclonic spiral eddies is observed in the submesoscale regime. The predominant cyclonic rotation, reported e.g. by Munk et al. (2000), is not fully understood yet and contrasts with a more symmetric balance between cyclones and anticyclones observed for mesoscale dynamics.

In this study we investigate the connection between spiral surface flow pattern in the ocean and their cyclonic rotation. We find that ageostrophic flow components in submesoscale dynamics lead to smaller sized cyclones, with enhanced horizontal velocity and pressure gradients. These sharpened horizontal gradients, which are not geostrophically balanced yield enhanced vertical velocities. Spiral structures can only evolve on a horizontally non-divergent velocity field and are thus also associated with enhanced vertical velocities, contrary to nearly two-dimensional mesoscale dynamics. In contrary the submesoscale anticyclonic regions have less enhanced gradients and vertical velocities and thus do not favour spiral structured eddies, but closed, vortex-like structures similar to mesoscale dynamics.

To study different dynamical regimes from submesoscale to mesoscale and to verify our hypothesis we use numerical simulations of the idealised python Ocean Model (pyOM, *Eden* (2011)). Several experiments are performed with initial conditions corresponding to mesoscale and submesoscale dynamics.

The simulated instabilities correspond to time and length scales predicted by linear stability analysis and are similar to observed baroclinic instabilities. Especially the cyclonic dominance in the submesoscale simulation is confirmed.

An analysis of pressure perturbation, relative vorticity and vertical velocities for different dynamical regions confirms our hypothesis of the coherence of cyclonic eddies and enhanced vertical velocities, as well as the different sizes of cyclones and anticyclones in the submesoscale regime.

Contents

1. Introduction

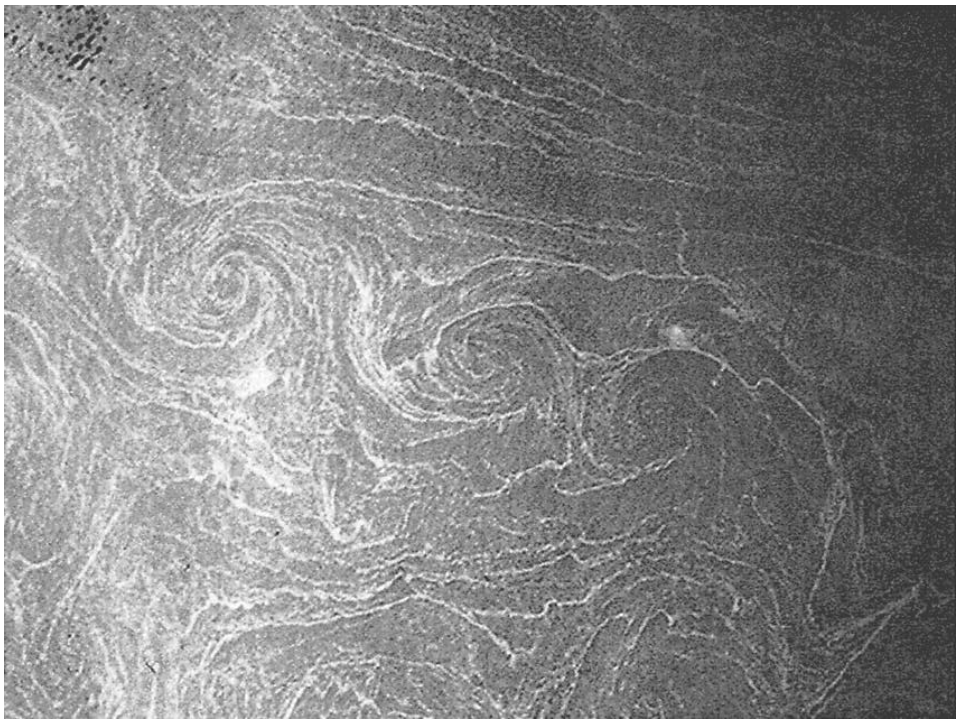

Figure 1.1.: *Photograph of a spiral eddy street in the Mediterranean Sea off the coast of the Egyptian/Libyan border (32.08N, 26.08E, north is upward). The diameter of the eddies is roughly 10 km. From Eldevik and Dysthe (2002), originally from Scully-Power (1986)*

In this thesis the process of baroclinic Mixed Layer Instabilities (MLIs), generating spiral eddies, is analysed with respect to their predominant cyclonic rotation sense, reported for example by *Munk et al.* (2000) and *Eldevik and Dysthe* (2002). At the beginning the importance of baroclinic instabilities in Mixed Layer (ML) dynamics is pointed out. This will be followed by an introduction to the phenomenon of spiral eddies and the actual state of research concerning cyclone-anticyclone asymmetry in ML dynamics. In the introduction into theory (chapter 1.3) the different dynamical regimes are characterised. Furthermore theoretical arguments concerning

the initial question of cyclonic favor are introduced.

The ML, with its approximately homogeneity of properties in the vertical, plays an important role in atmosphere-ocean interactions. Exchange of biogeochemical tracers, implying different greenhouse gases such as anthropogenic CO_2, buoyancy and potential vorticity, between ocean and atmosphere, as well as their vertical transport within the ML and beyond into the interior ocean, depends highly on ML properties and dynamics.

The dominant dynamical processes acting in the ML were long time assumed to be small scale turbulence and mesoscale motions, reducing vertical gradients and decreasing horizontal inhomogeneities, respectively. Since models and observations are able to capture also submesoscale ranges, which have spatial scales in between the small- and the mesoscales, this point of view has changed. About fifteen years ago, first studies (e.g *Haine and Marshall* (1998) and later on e.g. *Boccaletti et al.* (2007)) pointed out the importance of submesoscale processes in restratifying the ML and detected submesoscale dynamics as a leading order process for the buoyancy budget of the ML. Furthermore submesoscale processes are responsible for vertical transport of watermasses and thus also biogeochemical tracers below the ML into the intermediate ocean (*Thomas et al.*, 2008).
Lateral buoyancy gradients in the weak stratified vicinity of the ML are unstable to submesoscale baroclinic processes (e.g. *Boccaletti et al.* (2007)). They restratify the ML, in the way, that baroclinic instabilities evolve on strong horizontal density gradients, deminishing this gradients and leaving vertical gradients instead. State-of-the-art global models do not resolve submesoscale processes, hence miscalculating ML properties (*Boccaletti et al.*, 2007).
Understanding the process of submesoscale baroclinic instabilities will help to comprehend the restratification of the ML, thus helping to make better estimates of ML properties, like temperature and buoyancy distribution as well as ML depth, which is crucial to know for modeling ocean-atmosphere interactions.

The second decisive role of Mixed Layer Instabilities (MLIs) may found in their determining part in the energy cascade, which is not fully understood yet. *Thomas et al.* (2008) suggest that submesoscale instabilities (which are mainly balanced and well captured by hydrostatic equations, but arising on high Ro and low Ri) transfer energy to the larger scales, through the effect of growing eddies. Whereas the real ageostrophic instabilities (also called ageostrophic anticyclonic instabilities (AAI)) are more relevant to a forward energy cascade. It includes the transfer of energy from the mesoscale flow field via submesoscale processes to the small scales, where dissipation occurs (e.g. *Molemaker et al.* (2005) and *Skyllingstad and Samelson* (2012)).

1.1. Spiral eddies

The phenomenon of spiral eddies has been detected first in 1968 from crewed space flights, first thought to be a rare feature. Later spaceflights as well as satellite-born synthetic aperture radar (SAR) and infrared measurements give further evidence for high occurrence of submesoscale dynamics in general and spiral eddies in particular. For a more detailed history of the discovery of spiral eddies the reader is referred to *Munk et al.* (2000).

Already 40 years have passed since discovery, but the evolution process of spirals is not yet fully understood. Nowadays spiral eddies are assumed to be the surface signature of submesoscale baroclinic instabilities (compare e.g. *Eldevik and Dysthe* (2002)). Spiral eddies occur globally, with the exception of the equator. They belong to submesoscale dynamics implying horizontal scales of $\mathcal{O}$(1km). They are evolving in the ML, but can penetrate into the interior ocean, as has been shown by *Badin et al.* (2011). The surface pattern of those instabilities can be seen in figure 1.1. Typical for spiral eddies are shear lines with a width of roughly 100 m and a spacing between them of $\mathcal{O}$ $(1km)$ (*Munk et al.* (2000), *Eldevik and Dysthe* (2002); seen in figure 1.1 as white lines). Those streaks are visible in sun glitter

pictures and SAR-images due to convergence of biogenic slick, which dampens short wind-induced waves. The comparatively smoother sea surface leads to different back-scatter behaviour of radar and sunlight waves. More detailed information on the visibility of spiral eddies in remote sensing can be found again in *Munk et al.* (2000).

Spiral eddies occur often in an interconnected pattern, as can be seen in figure 1.1. Furthermore in some images a strong cyclonic displacement of ship tracks can be observed (*Munk et al.*, 2000). This is in agreement with the overwhelmingly cyclonic vorticity associated with spiral eddies (e.g. *Munk et al.* (2000), *Scully-Power* (1986)).

1.2. State of research

Munk et al. (2000) analyse over 400 images of spiral eddies, resulting in a lot of information concerning length- and timescales introduced in section 1.1. Furthermore they address the effect that makes spirals visible for remote sensing, additionally ruling out that cyclonic dominance is just a visibility effect.

In the second part of *Munk et al.* (2000) the question of cyclonic favour is adressed. Therefore the authors split the instability process into two separate simulations. First they consider a preconditioning phase where frontogenesis takes place. Two different front types are considered, an analytically softened Margules front and a time-dependent model of a Hoskins-Bretherton front (*Hoskins and Bretherton*, 1972). In this stage larger shears evolve (super-f shear) on the cyclonic side of the jet, than on the anticyclonic side. In a second process *Munk et al.* (2000) analyse the barotropic wound up of the shear into a spiral by shear instability, based on the Stuart solution (*Stuart*, 1967). The anticyclonic vortices experience the sub-f limit by inertial and gravitational instabilities. A mixture of inertial and gravitational instabilities, also called symmetric instability, arrises if absolute potential vorticity $Q \leq 0$. This means that symmetric instabilities arrise, when relative vorticity falls below $-f$ (compare equation 1.3). Summing up, *Munk et al.* (2000) found different

processes all favoring cyclonic vortices, but they did not figure out which one is the limiting one for anticyclonic vortices.

In contrast *Eldevik and Dysthe* (2002) simulate the entire evolution process of spiral eddies, reproducing cyclonic eddies consistent with observations and suggest spiral eddies to be the surface signature of ageostrophic baroclinic instabilities. Furthermore they introduce a theoretical argument for the cyclonic-anticyclonic asymmetry, which is shown and discussed below (compare eq. 1.6 and 1.7).

Roullet and Klein (2010) also revealed cyclonic dominance in a numerical simulation, explaining it due to active upper boundary effects, but lacking an explanation for the dominance beyond numerical simulations. They declare to find cyclonic dominance in contrast to previous studies referring to publications experiencing anticyclonic dominance like e.g. *Koszalka et al.* (2009), who are not describing an instability process emerging from a density front, but wind-forced turbulence of an initial resting fluid and e.g. *Cho and Polvani* (1996), whose simulations are not in the submesoscale range.

Studies concerning cyclonic-anticyclonic asymmetry can be found in meteorology as well (e.g. from observational data by *Klein* (1958)). *Hakim et al.* (2002) reproduce the tropopause cyclone-anticyclone asymmetry in size and strength in numerical simulations, by including ageostrophic terms in a surface QG approximation. An indication that spiral cyclones in the ocean also differ in size and strength from their anticyclonic counterparts is given by a regional study in front of the Norwegian coast (*Dokken and Wahl*, 1996).

1.3. Introduction into Theory

Submesoscale dynamics

Various definitions of submesoscale and ageostrophic dynamics are used, and in literature often ageostrophic is used synonymously with submesoscale, which leads to some confusion. We use the following definition of submesoscale dynamics. The

submesoscale dynamics are still mainly balanced, but ageostrophic terms start to play a role. The submesoscale regime can be characterised by the dimensionless numbers, introduced below.

Spiral eddies, as mentioned in the previous section, are restricted to the upper ocean and are among submesoscale dynamics. Conditions in the ML coincide in large parts with the criteria which are typically used to define submesoscale dynamics (which does not mean there is no submesoscale dynamic below the ML).

In the following part we want to focus on a differentiation between submesoscale and mesoscale regimes by means of the non-dimensional Richardson- and Rossby number. By varying different parameters in the numerical simulations they will be adjusted to those conditions.

For submesoscale conditions the relative vorticity ($\zeta = \partial_x v - \partial_y u$) has to be at least of the same order as the planetary one (f), hence quantifying the importance of the Coriolis force in the observed process. This leads to Rossby numbers (Ro) of:

$$Ro = \frac{\zeta}{f} \sim \mathcal{O}(1) \tag{1.1}$$

Analogue we can introduce the Richardson number (Ri), which indicates the importance of vertical shear with respect to stratification. In the submesoscale range the buoyancy frequency (N) and the vertical shear $\left(\frac{\partial \mathbf{u}_h}{\partial z}\right)$ has to be of the same order. The subscripted h denotes the horizontal components of velocity. This leads to Ri of:

$$Ri = N^2 \left(\frac{\partial \mathbf{u}_h}{\partial z}\right)^{-2} \sim \mathcal{O}(1) \tag{1.2}$$

Whereas typical values for mesoscale dynamics are $Ro \ll 1$ and $Ri \gg 1$. From $Ro \sim Ri \sim 1$ (for submesoscales) one can conclude that the planetary vorticity still plays an important role but is not as dominant as in the mesoscale range, where quasi-geostrophy can be assumed. From Ri ~ 1 we can conclude that vertical and horizontal processes have to be considered, in contrary to the mesoscale range which is assumed to be mainly 2-dimensional with diminishing vertical velocities.

Conservation of Ertel potential vorticity

The theoretical argument for cyclone-anticyclone asymmetry is based on the conservation of Ertel potential vorticity (EPV) (*Eldevik and Dysthe*, 2002)

$$Q = -\frac{1}{\rho_0}(\boldsymbol{\xi} + \boldsymbol{f}) \cdot \nabla\rho \tag{1.3}$$

In a stable stratified state we can always assume $Q > 0$, with static instabilities rising otherwise. Assuming conservation of potential vorticity ($\frac{DQ}{Dt} = 0$) and using the thermal wind equation (1.4 and 1.5)

$$f\frac{\partial v}{\partial z} = -\frac{g}{\rho_0}\frac{\partial \rho}{\partial x} \tag{1.4}$$

$$f\frac{\partial u}{\partial z} = \frac{g}{\rho_0}\frac{\partial \rho}{\partial y} \tag{1.5}$$

we obtain following inequality

$$\rho_0 Q \simeq -\frac{g}{\rho_0 f}\left|\nabla_H \rho\right|^2 - (f+\zeta)\frac{\partial \rho}{\partial z} \geq 0 \tag{1.6}$$

this leads to a lower boundary for the z-component of the relative vorticity ζ

$$f + \zeta \geq 0 \tag{1.7}$$

while no such boundary exists for positive values. The above mentioned argument was not devised by *Eldevik and Dysthe* (2002) but it is their main argument for cyclonic dominance in the submesoscale range.

Using the thermal wind equation in an argument for cyclone-anticyclone asymmetry in a submesoscale instability process might not be a completely valid approximation, because it uses the geostrophic balance. Furthermore the argument assumes conservation of EPV, although the ML is forced for example through buoyancy loss or gain.

Cyclostrophic balance

In this section a differentiation between mesoscale and submesoscale cyclones and anticyclones by means of the different force balances is presented. Equation 1.8 represents the balance of centrifugal, Coriolis and pressure force in cylindric coordinates.

Gradient-wind balance

$$-\frac{v^2}{r} - fv = -\frac{1}{\rho_0}\frac{\partial p}{\partial r} \tag{1.8}$$

with v the orbital velocity, r the vortex radius, p the pressure, ρ_0 the reference density and f the Coriolis parameter.

Now we introduce a scaling of equation 1.8 with $\hat{v}-$ the scaled orbital velocity v, $\hat{r}-$ horizontal length scale, $\hat{f}-$ Coriolis parameter$-$ and $\hat{p}-$ the pressure pertubation scale.

Scaled gradient-wind balance

$$\frac{v^2}{r}\frac{\hat{v}^2}{\hat{r}} - fv\hat{f}\hat{v} = -\frac{1}{\rho_0}\frac{\partial p}{\partial r}\frac{\partial \hat{p}}{\partial \hat{r}} \tag{1.9}$$

Now we devide by fv and with the assumption of a dominant geostrophic balance the Coriolis force term and the pressure force term are equal and thus after deviation one. If we now introduce the global $Ro = \frac{v}{rf}$ equation 1.9 looks the following

$$-Ro\frac{\hat{v}^2}{\hat{r}} - \hat{f}\hat{v} = -\frac{1}{\rho_0}\frac{\partial \hat{p}}{\partial \hat{r}} \tag{1.10}$$

The importance of the third term, the Centrifugal force, depends on the Ro. Mesoscale dynamics are associated with low Ro ($Ro \ll 1$) and hence the Centrifugal force is neglectable. Therefore the geostrophic balance (equation 1.11) is an appropriate simplification to describe mesoscale vortices. In the submesoscale regime $Ro \approx \mathcal{O}(1)$ and thus the Centrifugal force becomes as important as the Coriolis force and the pressure force.

Geostrophic balance

$$-fv = -\frac{1}{\rho_0}\frac{\partial p}{\partial r} \tag{1.11}$$

The force balances in mesoscale vortices are depicted in the upper part of figure 1.2. Assuming equal pressure perturbations and velocities for low and high pressure systems, pressure force and Coriolis force are identical in both pressure systems, only

acting in opposed directions. This results in equal sized cyclonic and anticyclonic vortices for low and high pressure anomalies, respectively.

For vortices with Rossby number of $\mathcal{O}(1)$ no term of equation 1.8 is negligible. The centrifugal force is always directed outward of a rotating pressure system. In a low pressure system it is thus balancing partly the inward directed pressure force, contrary to a high pressure vortice of intermediate size. Here the centrifugal force and the pressure force are both directed outward and have to be balanced by the Coriolis term. This leads to higher orbital velocities for high pressure vortices of same size and pressure anomaly as for low pressure vortices, or equivalently to larger anticyclones for same pressure anomalies and orbital velocities (compare figure 1.2).

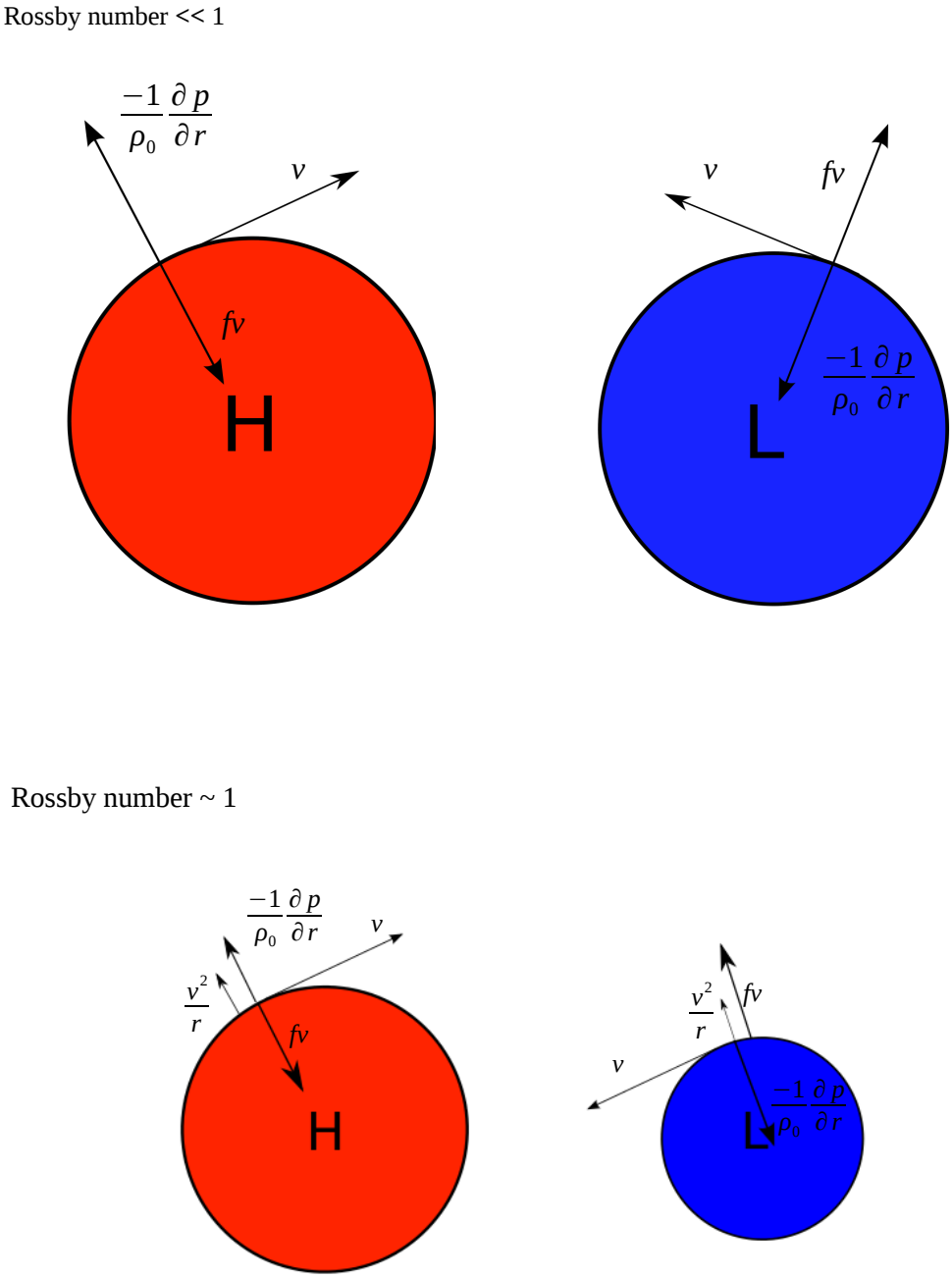

Figure 1.2.: *Balance between the different terms of equation 1.8, after Cushman-Roisin and Beckers (2011) chapter 18. For the larger mesoscale dynamics ($Ro \ll 1$) in the upper part and for the smaller submesoscale dynamics ($Ro = \mathcal{O}(1)$) in the lower part.*

Structural differences of mesoscale and submesoscale eddies

The different structure of vortices in dependency of the divergence of the flow field, was already introduced by *Okubo* (1970). In a non-divergent flow field vortices have to build closed circulation patterns, called vortices (compare 1.3). Spirals can only evolve in a divergent flow field. Divergent flow fields are associated with enhanced vertical velocities, that transport downward (upward) the converging (diverging) water. It is well known that mesoscale dynamics are assumed to be 2-dimensional

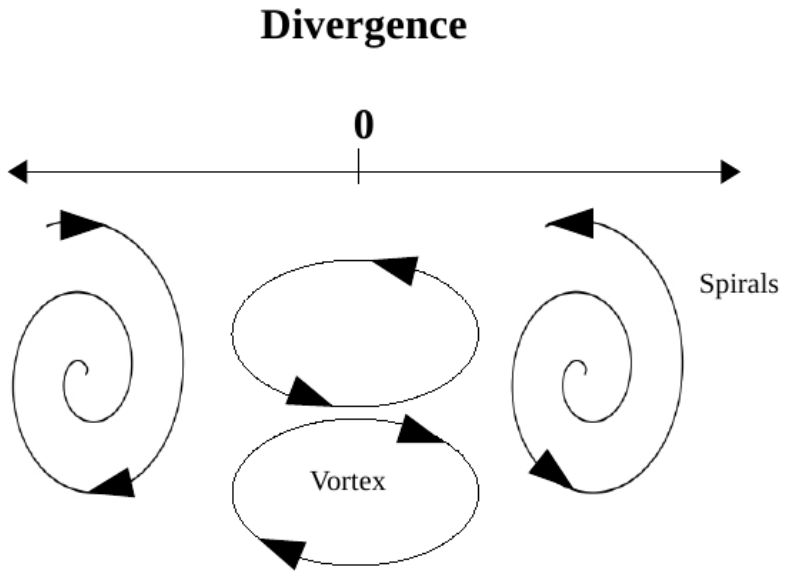

Figure 1.3.: *Different structures of eddies, in dependence of the divergence of the flow field, after Okubo (1970)*

with negligible vertical velocities, while submesoscale dynamics are associated with enhanced vertical velocities. Additionally this can be concluded from the vorticity equation (1.12) derived as follows from the inviscid horizontal momentum equations ($\beta-$effects are neglected).

$$\frac{Du}{Dt} - fv = -\frac{1}{\rho_0}\frac{\partial p}{\partial x} \qquad \left| \cdot \left(-\frac{\partial}{\partial y}\right) \right.$$

$$\frac{Dv}{Dt} + fu = -\frac{1}{\rho_0}\frac{\partial p}{\partial y} \qquad \left| \cdot \left(\frac{\partial}{\partial x}\right) \right.$$

Taking the curl of the horizontal momentum equation reveals:

$$\frac{\partial u}{\partial x} + \frac{\partial v}{\partial y} = -\frac{1}{f}\frac{D}{Dt}\left(\frac{\partial v}{\partial x} - \frac{\partial u}{\partial y}\right) \tag{1.12}$$

Using the continuity equation ($-\frac{\partial w}{\partial z} = \frac{\partial u}{\partial x} + \frac{\partial v}{\partial y}$) and the relative vorticity ($\zeta = \frac{\partial v}{\partial x} - \frac{\partial u}{\partial y}$) equation 1.12 becomes the following:

$$-\frac{\partial w}{\partial z} = -\frac{1}{f}\frac{D\zeta}{Dt} \tag{1.13}$$

The left hand side of equation 1.13 gives the change of vertical velocity with depth. The term on the right hand side of equation 1.13 is small in mesoscale regimes, leading to small $\frac{\partial w}{\partial z}$. In contrary in submesoscale dynamics the advective derivative of ζ (right hand side of equation 1.13) is not neglectable in submesoscale dynamics, leading to larger $\frac{\partial w}{\partial z}$.

Thus we are expecting vortex structures to evolve in mesoscale simulations and spiral structures in submesoscale simulations.

1.4. Hypothesis

Based on the introduced previous studies and arguments, this thesis tries to further investigate the cyclonic dominance in ML baroclinic instabilities.

To realise this, the transition between mesoscale and submesoscale processes (characterised by typical Ri and Ro) is investigated with respect to cyclone-anticyclone occurrence.

In principle there seem to be two possibilities for cyclonic dominance. First option would be a qualitative difference already in the beginning of the instability process, i.e. less anticyclones evolve. The second possibility is that anticyclones get unstable at some stage of the process and thus more cyclones are to be observed. Nevertheless the main question of this thesis is the following.

Why do submesoscale ranges exhibit an asymmetry of cyclones and anticyclones, whereas mesoscale eddies feature a more symmetric distribution?

We assume that structural and spatial discrepancies of cyclones and anticyclones in

the different dynamical regimes are responsible for this asymmetry. To fortify this hypothesis, numerical simulations of baroclinic instability processes in mesoscale, intermediate and submesoscale regimes have been performed. To confirm the expected behaviour of baroclinic instabilities to convert available potential energy into eddy kinetic energy, the energy developement over time is considered . Afterwards temperature and velocity fields are presented to give a rough overview of the structural discrepancies in the different dynamical regimes. Length and time scales and depth structure of perturbation velocity and buoyancy, predicted by linear stability analysis, are compared with the emerging instabilities in the simulations. Furthermore they are set into relation with observations of length and time scales, for the particular regimes, to confirm that the simulated instabilities represent the processes we want to investigate further.

The importances of geostrophic and ageostrophic velocity components are considered seperately to verify the arguments of different sizes for cyclones and anticyclones in submesoscale regimes from the Gradient Wind Balance (section 1.3).

Afterwards the Okubo-Weiss-parameter is introduced to identify eddies. Using the Okubo-Weiss-parameter the structure of the vertical velocity and relative vorticity is associated with the eddies, verifying the structural differences of eddies in divergent and non-divergent flow fields (compare section 1.3). This leads us to our main hypothesis, that due to different force balances in mesoscale and submesoscale regimes the size of cyclones and anticyclones is the same in mesoscale dynamics, while larger anticyclones and smaller cyclones evolve in submesoscale ranges (section 1.3). In the larger anticyclones horizontal gradients are weaker than in smaller cyclonic eddies. Associated with the enhanced gradients in cyclonic regions are higher vertical velocities. This implies that cyclonic eddies form spiral structures, whereas anticyclones feature lower vertical velocities and cannot develope spiral structures.

2. Model description and Methods

For the numerical simulation the idealised python Ocean Model (pyOM) was used, as described in *Eden* (2011). The model equations and a description of the set-up and the initial conditions can be found in the following chapter. An overview of all realised experiments and varied parameters can be found in table 2.2.
The second part of this chapter consists of a short description of linear stability analysis for submesoscale conditions, which will be used in various contexts.

2.1. Model Equations

In the pyOM the Navier-Stokes-equations, density- and volume conservation equations in Boussinesq-approximation are solved. In this case also the hydrostatic approximation is made (which is valid in the submesoscale range to $\mathcal{O}\ (Ro^2 H/L)$; (*Thomas et al.*, 2008)) and constant f is assumed:

$$\begin{aligned}
\frac{\partial u}{\partial t} &= fv - \vec{u}\cdot\nabla u - \frac{\partial p}{\partial x} + \mathcal{F}_x \\
\frac{\partial v}{\partial t} &= -fu - \vec{u}\cdot\nabla v - \frac{\partial p}{\partial y} + \mathcal{F}_y \\
0 &= -\frac{\partial p}{\partial z} - b \\
\frac{\partial b}{\partial t} &= -\nabla\cdot(\vec{u}b) + K_h\nabla_h^2 b + K_v\frac{\partial^2 b}{\partial z^2} \\
\nabla\cdot\vec{u} &= 0
\end{aligned} \tag{2.1}$$

where pressure p and buoyancy b are scaled with the constant reference density ρ_0. $\mathcal{F}_x$ and $\mathcal{F}_y$ contain the horizontal and vertical harmonic and biharmonic friction terms. For the presented simulations only harmonic friction is used. K_h and K_v denote the horizontal and vertical diffusivity, respectively. The horizontal diffusion

was realised by a quicker advection scheme.

The discretisation of the variables is on an Arakawa-C-grid, with p and b centered in the middle, u, v and w are placed at the eastern, southern and upper side of the grid. The boundary conditions are chosen as follows. At the surface the rigid lid boundary condition is applied, while for the lower boundary a flat bottom is used. In x-direction we assume periodic boundary conditions, whereas the boundaries are closed in y-direction. At the meridional boundaries and the bottom noslip conditions apply.

2.1.1. Parameter analysis to distinguish between submesoscale and mesoscale dynamics

In this section the reader will find a short summary about the chosen parameters, which qualitatively define the submesoscale and the mesoscale dynamics. Therefore a scaling of the equations of motion has to be applied, as done by *Brüggemann and Eden* (2012) (personal communication). This leads to a set of equations scaled with the non-dimensional parameters $Ro = \frac{U}{\Omega L}$, $Ri = \frac{N^2 H^2}{U^2}$ and the aspect ratio $\delta = \frac{H}{L}$, where U denotes horizontal velocity scales, Ω the Coriolis parameter, L horizontal length scales, N^2 the vertical buoyancy gradient and H vertical length scales. Assuming now that horizontal length scales are at the order of the Rossby radius leads to $Ri = \frac{1}{Ro^2}$, leaving only two independent parameters that can be varied to achieve the different dynamics. In submesoscale dynamics Ro and Ri are assumed to be $\mathcal{O}(1)$, furthermore a larger aspect ratio δ is expected, while for mesoscale conditions $Ro \ll 1$ and $Ri \gg 1$ and a smaller aspect ratio δ are valid assumptions.

In accordance to this, the parameter for the different experiments are chosen as listed in table 2.3. The Coriolis parameter is set to 10^{-4} s^{-1} for all simulations, representing a typical mid-latitude value. The geostrophically balanced background velocity U gives the typical horizontal velocity scale and is set to 0.2 ms^{-1} in all regimes.

From the given Ro and δ and the number of discretised gridpoint the domain size

and resolution given in table 2.2 can be calculated. Furthermore all parameters to initialise the model can be calculated as follows.

Parameter	Calculation
L	$\frac{U}{\Omega Ro}$
H	δL
Ri	$\frac{1}{Ro^2}$
N	$\sqrt{\frac{RiU^2}{H^2}}$
M_0	$-\text{sign}(U) \cdot \frac{Ro}{\delta} \cdot \Omega^2$
dx	$\frac{L}{n_x}$
dy	$\frac{L}{n_y}$
dz	$\frac{H}{n_z}$

Table 2.1.: Calculation of all further parameters required to initialise the numerical simulations from given Ro, δ, U_0 and Ω

2.1.2. Set-up

For experiments 1, 2, 4 and 5 in both horizontal directions 256 gridpoints and 80 vertical layers are discretised. Furthermore one lower resolution experiment (3) is shown, since some results can be seen more obviously in this simulation. The resolution and the used viscosities of each experiment can be seen in table 2.2. The width and length of the model domain are chosen such that four to seven initial pertubations can grow.

For the submesoscale regime two different types of buoyancy gradients are realised. In the first case a linear gradient is simulated, thus one can compare it more easily to the mesoscale and the intermediate experiment. The second simulation is initialised with a hyperbolic tangent shaped buoyancy gradient, which fits better the sharpened horizontal buoyancy fronts and the vertical buoyancy structure of a ML.

exp	Scale	resolution [m]		gridpoints		viscosity	
		horizontal	vertical	horizontal	vertical	horizontal	vertical
1 & 2	submesoscale	250	1	256	80	40	$7 \cdot 10^{-5}$
3	submesoscale	625	2.5	128	40	19.5	$6.25 \cdot 10^{-5}$
4	mesoscale	$1.25 \cdot 10^{4}$	12.5	256	80	$1.5 \cdot 10^{3}$	$4 \cdot 10^{-4}$
5	inter	$1.25 \cdot 10^{3}$	2.5	256	80	90	$1.5 \cdot 10^{-4}$

Table 2.2.: Resolution, discretisation and viscosity for all presented experiments

Since this structure is not representative for mesoscale conditions, in the mesoscale and the intermediate case only linear gradient simulations have been performed.

2.1.3. Initial conditions and realised experiments

The initial conditions for experiment 2 can be seen in figure 2.1. In the left figure (a) surface temperature (colour) and velocity (arrows) are shown for the first time step, while the right figure (b) shows an along-stream section of the domain.
The domain is preconditioned with a lateral buoyancy gradient as well as a geostrophically balanced zonal jet. All simulations are realised on a f-plane, thus no spatial variation of the Coriolis force is possible. Furthermore all experiments are unforced, i.e. are spin-down experiments. See below at table 2.3 for details about parameter variations. In vertical direction the density stratification is given by the Brunt-Väisälä frequency N. Equivalently the horizontal buoyancy gradient is given by M_0. Furthermore a normal distributed random perturbation is applied on the buoyancy field of the whole domain.

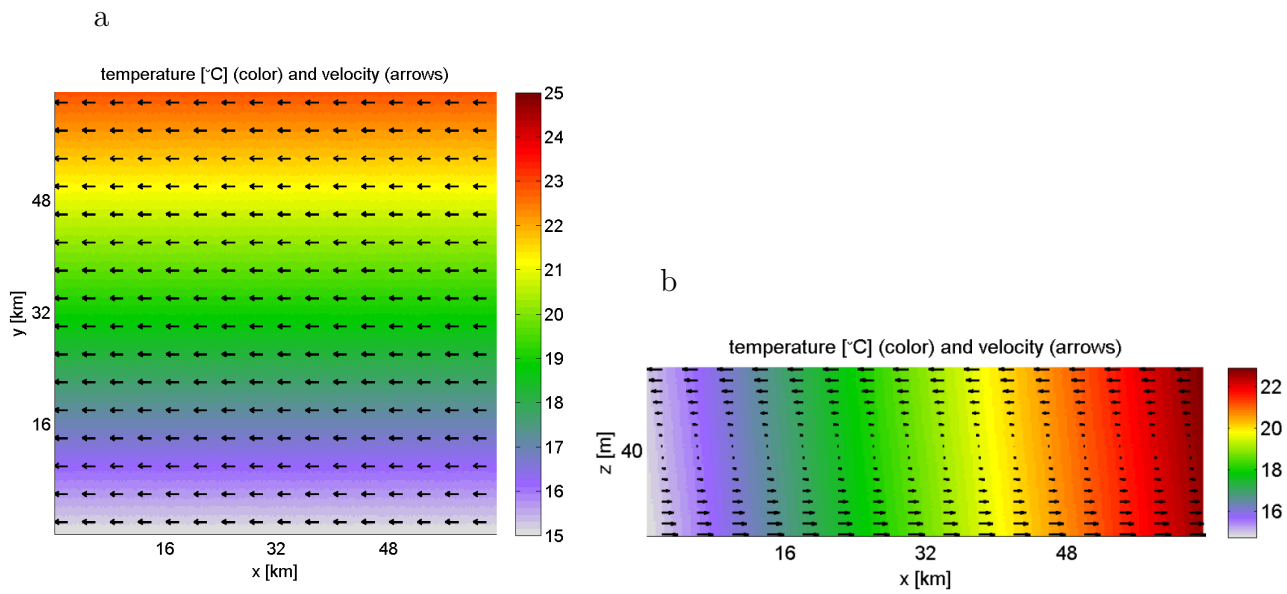

Figure 2.1.: *Initial temperature (color) and velocity (arrows) for the submesoscale simulation (experiment 2 in table 2.3), at the surface in (a) and for an along-stream section in (b).*

exp	scale	buoyancy gradient		N	U_0	Ro	Ri	f_0	δ
		type	$\frac{dT}{dz}$ [°C/km]	[1/s]	[m/s]			[1/s]	
1	submesoscale	nonlinear	max 0.37	0.002	0.2	-	-	$1 \cdot 10^{-4}$	0.04
2	submesoscale	linear	0.13	0.0025	0.2	1	1	$1 \cdot 10^{-4}$	0.04
3	submesoscale	linear	0.10	0.0025	0.2	0.8	1.56	$1 \cdot 10^{-4}$	0.04
4	mesoscale	linear	0.01	0.01	0.2	0.02	2500	$1 \cdot 10^{-4}$	0.01
5	inter	linear	0.05	0.005	0.2	0.2	25	$1 \cdot 10^{-4}$	0.02

Table 2.3.: Realised experiments and the implemented parameters, defining different dynamical regimes. For explanations concerning the chosen parameters see section 2.1.1

2.2. Linear stability analysis

In this part the linear stability problem for submesoscale regimes will be introduced, followed by a description for what purpose these analysis will be used.
The following set of equations in the Boussinesq-approximation (the pressure term

related to sound waves in the continuity equation is kept for later use here) are used together with an f-plane approximation.

$$\begin{aligned}
&\frac{\partial u}{\partial t} + \vec{u} \cdot \nabla u - fv + f_h w = -\frac{\partial p}{\partial x} \\
&\frac{\partial v}{\partial t} - \vec{u} \cdot \nabla v + fu = -\frac{\partial p}{\partial y} \\
&\frac{\partial w}{\partial t} + \vec{u} \cdot \nabla w - f_h u = -\frac{\partial p}{\partial z} - b \\
&\frac{\partial b}{\partial t} + \vec{u} \cdot \nabla b = 0 \\
&c_s^{-2} \frac{\partial p}{\partial t} + \nabla \cdot \vec{u} = 0
\end{aligned} \tag{2.2}$$

These equations are linearised for a background velocity $\vec{u}$, buoyancy b and pressure p, in the form $x_i = X_0 + x'$, where $\vec{U_0} = (U_0, 0, 0)$. Afterwards a waveansatz is made again for $\vec{u}$, b and p of the kind $x_i = x_{i,0}(z) exp\ i(wt - kx - ly)$, which leads to an z-depending eigensystem of the following form $\omega a(z) = M(z)a(z)$.

This eigensystem can be solved numerically and eigenvectors and eigenvalues for each z-level are obtained. From the eigenvectors, vertical structure functions for $\vec{u}$, b and p can be derived, while the eigenvalues can be used to calculate the fastest growing perturbation in dependency of the wavenumber.

In a zonal channel it is assumed, that the fastest growing wave is not propagating in meridional direction. Thus the dependency of the fastest growing mode is calculated only in dependency of the zonal wavenumber.

The vertical eigenvectors (structure functions) give the relative amplitude of the considered property with depth. The total amplitude can not be derived directly by Linear Stability Analysis. Nevertheless the relative amplitude can be scaled with the typical time and length scales, given by the maximal growth rate and the fastest growing wavenumber. The complete solution can then be calculated as $x_i(x, z) = |a(z)| \sin(k_{\max} x - \omega_{\max} t + \arg(a(z)))$.

The submesoscale growth rate in dependancy of the scaled zonal wavenumber is shown in figure 2.2. The maximum growth rate of the blue curve is used to obtain a parameter independent time measurement and all time dependent developments

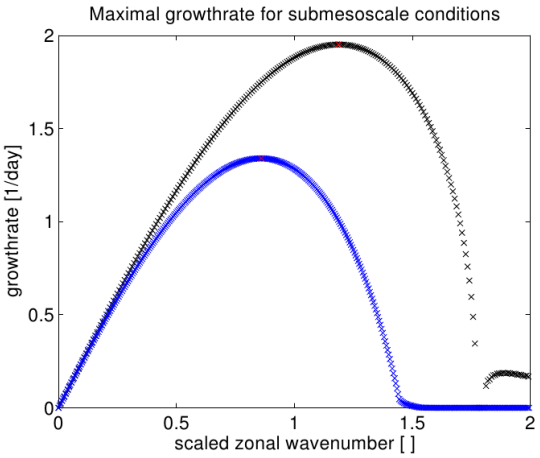

Figure 2.2.: *Growth rate as a function of the scaled zonal wavenumber for submesoscale conditions (experiment 2 in table 2.2). The black curve shows the inviscid growth rate, while the blue curve represent the growth rate predicted for the simulation with the friction mentioned in table 2.2.*

in this thesis are given in growth rates. The blue curve reprents the growth rate expected for the simulation, while the black curve show the growth rate for inviscid conditions. The predicted length and time scales as well as the depth structures of buoyancy and velocity perturbation are used to verify that the simulated instabilities correspond with observed submesoscale and mesoscale eddies.
The theory and the numerical code for the Linear Stability Analysis was provided by Prof. Dr. Carsten Eden (pers. communication).

3. Results

In this chapter selected model runs, mainly one submesoscale, one mesoscale and one intermediate simulation, will be presented, analysed and compared. The submesoscale results, if not stated different, refer therby to experiment 2 (compare table 2.2 and 2.3). Additionally some results from two other submesoscale simulations are shown, one with a non-linear buoyancy gradient (experiment 1 in table 2.2) and a lower resolution run (experiment 3 in table 2.2).

The chapter begins with a consideration of the phases of the instability process in section 3.1, therefore the time dependent behavior of kinetic and potential energy is shown, as well as representative plots of temperature and velocity fields. The length- and time scales as well as the structure of the developing instabilities are compared with the results of a Linear Stability Analysis (LSA) in section 3.2. Therefore amongst others the results of a spectral density estimate of the kinetic energy are used, to confirm that the simulated instabilities are representative for observed ones and can be used to investigate the main hypothesis.

Time series of Ri and Ro are used to characterise the dynamical regimes. Thereby $Ro \approx Ri \approx 1$ represent submesoscale dynamics, while $Ro \ll 1$ and $Ri \gg 1$ characterise mesoscale regimes. To examine the question of cyclonic favour, statistical properties of the local Rossby number are presented in section 3.3.

To give an estimate, which terms of the equations of motions play a decisive role in the different regimes, the ratio between geostrophic and ageostrophic velocity components is illustrated.

Afterwards eddies are identified using the Okubo-Weiss-parameter (OK) to give qualitative answers concerning the surface signature of eddies in the different dynamical regimes. Furthermore structure of vertical velocity, vorticity and pressure perturbation can be associated in this way, with eddies.

3.1. Phases of the process

To give an overview of the process first the evolution of kinetic and potential energy with time is shown. Furthermore temperature and velocity fields at characteristic stages of the process are presented for the different regimes.
The development of energy with time is shown only for the submesoscale regime, because no major differences exist for the different regimes; all simulations hold the same characteristic phases, marked in figure 3.1. We introduce an universal time scale, the growth rate predicted by LSA, to obtain a parameter independent time measurement (theory in section 2.2).
Maximal growth rates for each regime are calculated in section 3.2. In this way the time axis for all regimes is very similar, while the mesoscale simulation covers three years, whereas the submesoscale experiment is simulated only over 50 days.

Eddy Kinetic Energy (EKE) is calculated as $\int \overline{\frac{1}{2}(u'^2 + v'^2)}$, where x' denotes the deviation from the zonal mean $\overline{x}$. The total potential energy (PE) is given by $\int \overline{b \cdot dz}$, with b - buoyancy and dz- depth increment. The available potential energy (APE) is calculated as difference between minimal possible potential energy (MPE) and PE. MPE in this case is the state with the lowest possible potential energy. Therefore all buoyancy values are sorted ascendingly (b') and a new depth increment $dz_{new} = \frac{dx \cdot dy \cdot dz}{L_x \cdot L_y}$ is calculated. MPE is than given by $\int \overline{b' \cdot dz_{new}}$.

Baroclinic instabilities are assumed to convert APE to EKE. Thus we can expect an increase in EKE during the instability process with a simultanious decrease of APE. This is in good agreement with the energy time series of the simulation in figure 3.1. Total Kinetic Energy (KE) increases strongly during the beginning of the instability process, reaching its maximum after 25 growth rates and decreases when no new eddies are formed. Responsible for this is the increasing EKE, while only few energy is transferred to the mean flow (not shown) by the instabilities. The total Potential Energy (PE) decreases at the same time, when the KE starts increasing, after about ten growth rates (compare 3.1). The decrease in PE comes

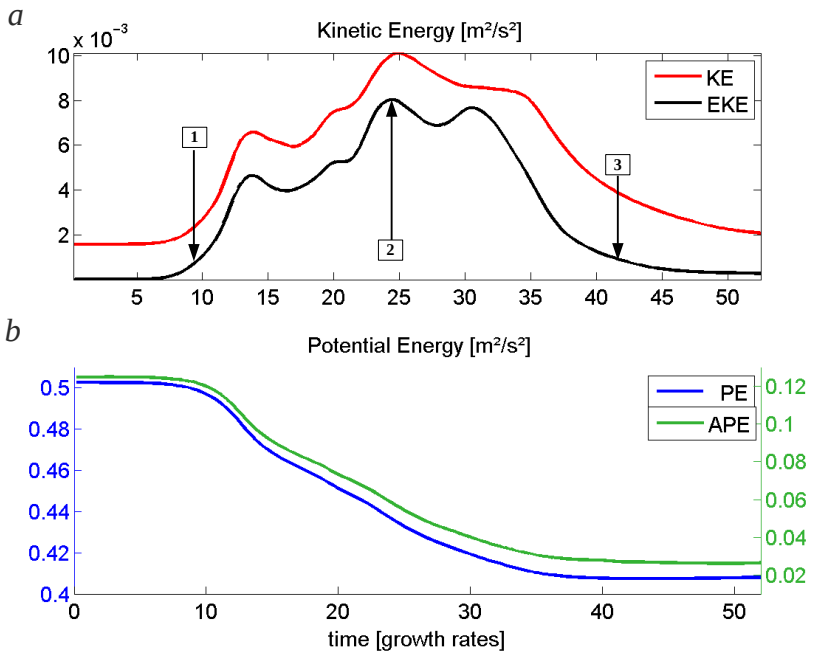

Figure 3.1.: *Kinetic and potential energy for the submesoscale simulation. (a) Total Kinetic Energy (red) and Eddy Kinetic Energy (black) are shown. The arrows mark characteristic stages of the process (for description see text below). (b) Total Potential Energy (blue) and Available Potential Energy (green).*

from a decrease in the APE. The effect of baroclinic instabilities to flatten isopycnals can well be recognised in figure 3.1 b, leading to APE values near zero at the end of the instability process. When no APE is left (after approximately 30 growth rates) EKE is on highest level and afterwards the instability process stops (spin-down experiments). Characteristic stages of the instability process can be recognised from this development of EKE and APE and following snapshots of diverse parameters are taken at the marked points. We define the time before EKE increases and APE decreases as the initial linear phase (begin to first arrow in figure 3.1 (a)), the turbulent instability process (first to second arrow) and the decaying phase (second arrow to third arrow).

The following figures 3.2 and 3.3 show snapshots of surface temperature and velocity fields for each simulation and each phase of the process. The left figures (a,

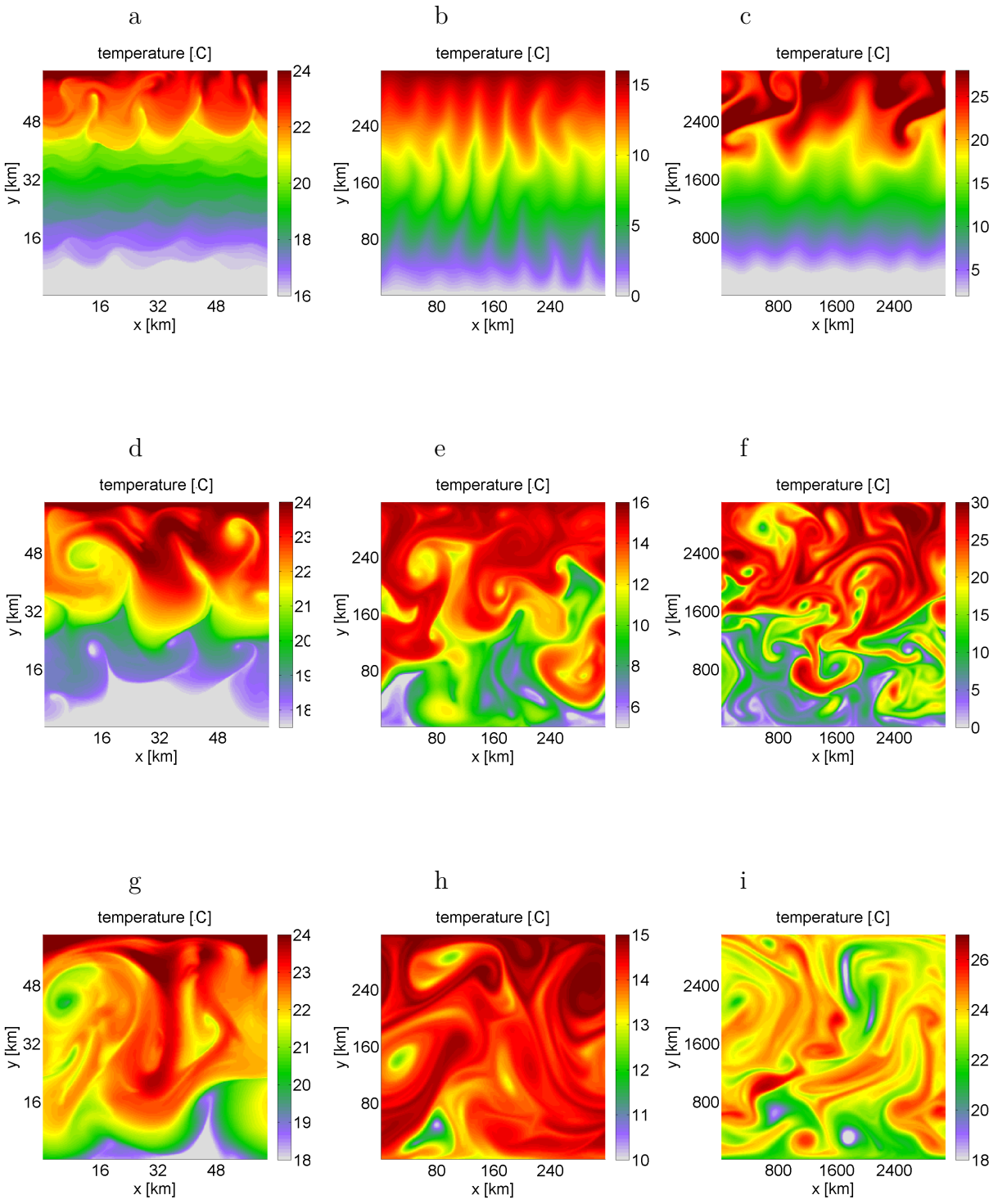

Figure 3.2.: *Surface temperature fields in a submesoscale (left), intermediate (middle) and mesoscale (right) simulation. (a,d,g) for the initial linear phase, (b,e,h) for the turbulent phase and (c,f,i) for the decaying phase*

d and g) are snapshots from the submesoscale simulation, in the middle (b, e and h) represent intermediate scale dynamics, while the right figures (c, f and i) show the corresponding temperature and velocity of the mesoscale simulation. The upper most figures (a-c) represent the end of the initial linear phase (compare arrows in figure 3.1), the middle ones (d-f) correspond to the turbulent instability process, while the lower most (g-i) temperature and velocity fields represent the decaying phase.

Different patterns of temperature can be observed for the meso- and the submesoscale regime already at the end of the linear phase, when the wave starts breaking (3.2 (a-c)). The breaking of the wave is already asymmetric in the submesoscale simulation. On the warm side spikey and long perturbations separate, while on the colder side the perturbations are rounded and expanded. Later on (d-f), in the submesoscale simulation the structure of the temperature perturbations is filament-like, contrary to the mesoscale case, where the eddies form a more closed circulation pattern, in the intermediate case a mixture between both of these structures can be observed. At this point eddies of all simulations have already fully evolved. This can be recognised from the high velocities as well as from the turbulent pattern of the temperature field, where no longer a clear wave pattern is visible (in the submesoscale simulation this is not entirely true, because the process starts at different times in the domain, thus in the southern part of the domain the wave structure is still visible). While in the mesoscale case warm and cold eddies, of equal size, separate from the meandering temperature field, in the submesoscale simulation only colder eddies separate in the warmer surrounding.

The cold perturbations are associated with cyclonic movements, as can be seen in figure 3.3 (a,d and g). One anticyclone is evolving at this snapshot, but stays not stable, gets influenced and finally disbanded by the surrounding cyclonic spirals.

In the intermediate simulation both, cyclones and anticyclones evolve but the flow field is dominated by cyclones. In the mesoscale case both, cyclones and anticyclones are found in equal number (figure 3.3 (f)). The last figures (3.2 and 3.3 (g,h and i)) show lower velocities again and a break down of the eddies. In the submesoscale

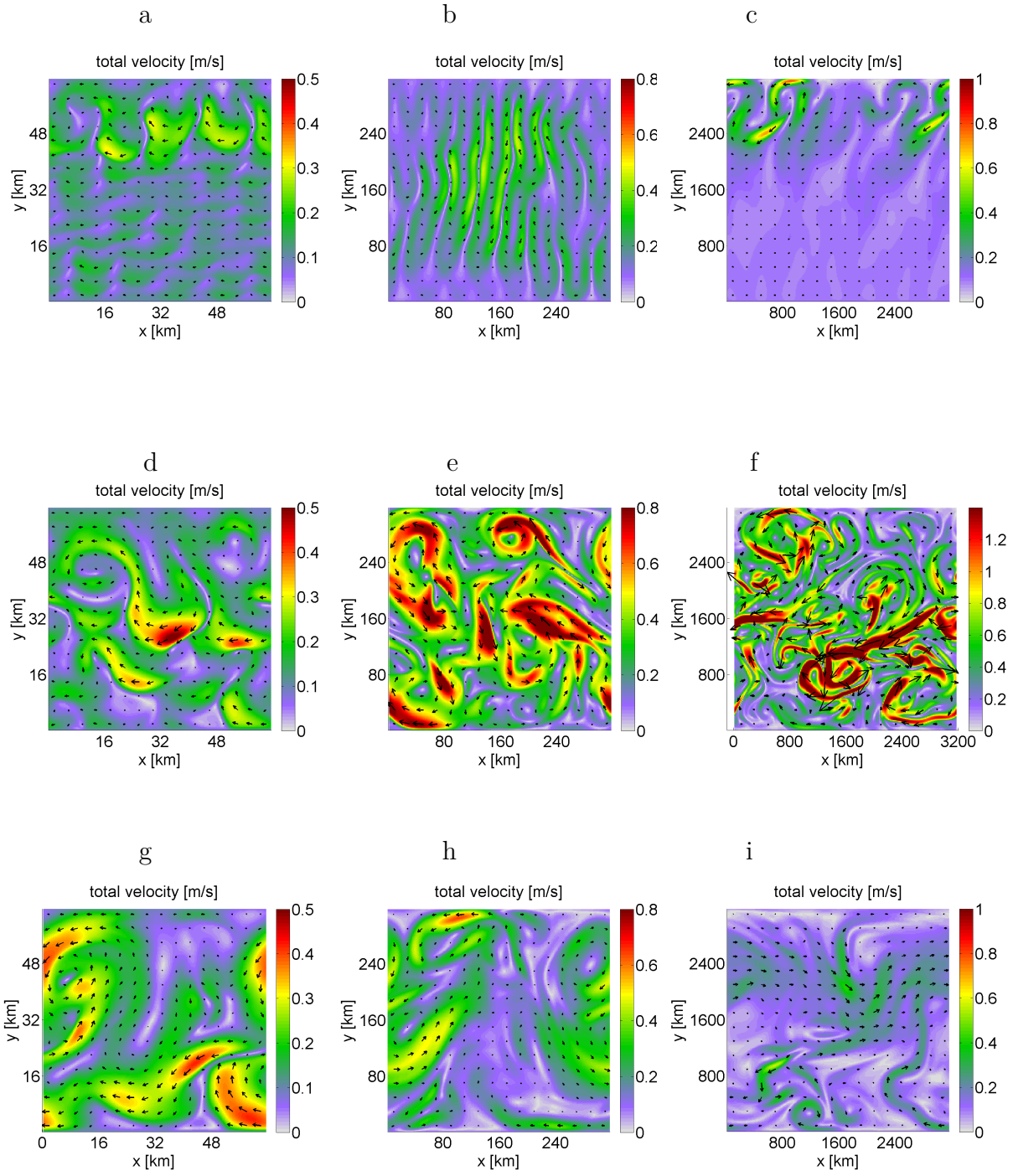

Figure 3.3.: *Surface velocity fields in a submesoscale (left), intermediate (middle) and mesoscale (right) simulation (a,d,g) for the initial linear phase (b,e,h) for the turbulent phase (c,f,i) for the decaying phase. The colour gives the amplitude of the horizontal velocity, the arrows the direction.*

perturbation and the region where the cold water originates from is visible, representing the spiral structure. Whereas the cold and warm perturbations in the mesoscale and the intermediate simulation are already completly uncoupled from their origin. The range of surface temperature is clearly decreased, due to the eddy activity, which deminished horizontal temperature gradients by restratifying the temperature front.
The colorbars of the different simulations are not the the same, because of different ranges. The scaling of the velocity arrows is equal within one experiment, but differs between the different experiments. The ratio of the vector length is (5:3:3) for (submesoscale: intermediate: mesoscale).

In figure 3.4 temperature of an across-stream section of the submesoscale simulation is depicted to visualise the frontal collaps, initialised by baroclinic instability. Figure (a), (b) and (c) represent the initial, the turbulent and the deacying phase, respectively. In the initial phase the isopycnals are still nearly vertical. The eddies convert the APE into EKE by restratifying these vertical gradients, leading to nearly horizontal isopycnals in the decaying phase (c). The change of vertical to horizontal isopycnals by baroclinic instabilities is also observable in mesoscale and intermediate experiments (not shown).

a

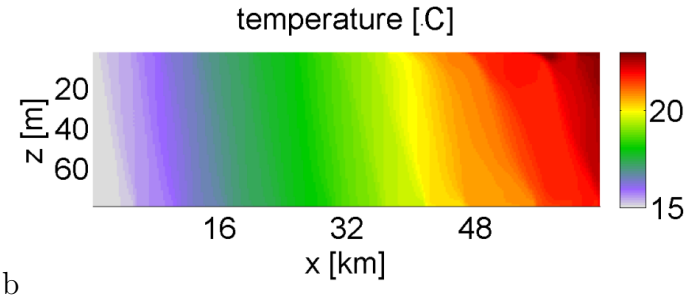

b

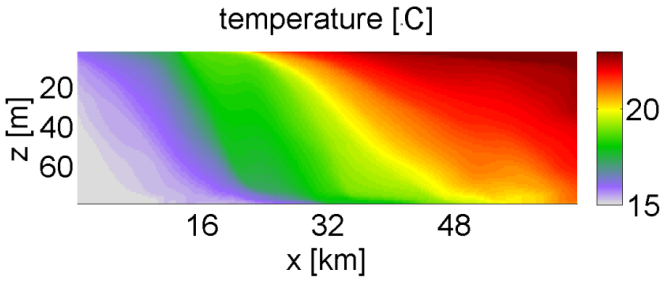

c

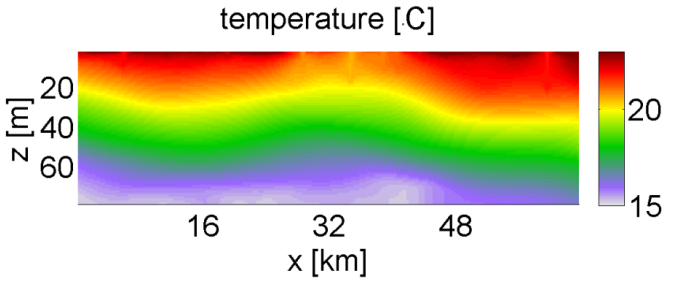

Figure 3.4.: *Submesoscale: Temperature of an along-stream section for the initial phase (a), the turbulent phase (b) and the decaying phase (c)*

3.2. Linear stability analysis predicts submesoscale instabilities

To predict length and time scales and the depth structure of the instability process, a linear stability analysis is applied (compare section 2.2). For the LSA we used the same background conditions (e.g. background velocity, horizontal and vertical buoyancy gradient and friction). The results of the LSA are set into relation with the simulated results and length and time scales from observations, to confirm that the simulations represent the instability processes we want to investigate. The corresponding length and time scales of the simulation represent always the end of the initial linear phase.

The predicted submesoscale length scale of LSA is presented in figure 3.5 *a*, disturbances around the scaled wavenumber 0.86 will grow fastest and thus dominating the wave field. This scaled wavenumber corresponds to a wavelength of 1.7 km. The wavenumber is scaled with the initial length scale $L_0 = \frac{N \cdot H}{f}$ of each simulation. To compare this result with length scales in the simulation a 1D Fast Fourier Transformation (FFT) has been performed, for the end of the initial linear phase. On the KE of each zonal section a FFT has been applied, calculating afterwards the mean of all zonal sections and its standard deviation. The result for the surface layer is depicted in figure 3.5 *b*. Also shown is the Rossby radius $R_d = \frac{N \cdot H}{f\pi}$ (green line), which is 640 m for the presented regime. This is a reasonable value for a ML Rossby radius of deformation. For the bottom layer the spectrum appears very similar (not shown) while in the intermediate layers (not shown) no distinct peak is visible, which is due to low horizontal velocities at mid depth (compare figure 3.8). The dominant scaled wavenumber is 0.98, corresponding to a slightly longer wavelength ($\approx$1.9 km) than the predicted one. This is due to the fact, that only discrete values of wavenumbers are possible (restricted by the domain size) and the predicted wavelength lies in between two realisable wavenumbers.

The standard deviation of the mean of all along-stream section wavenumber spectra is as high as the mean itself. One reason for this is the different starting time of the

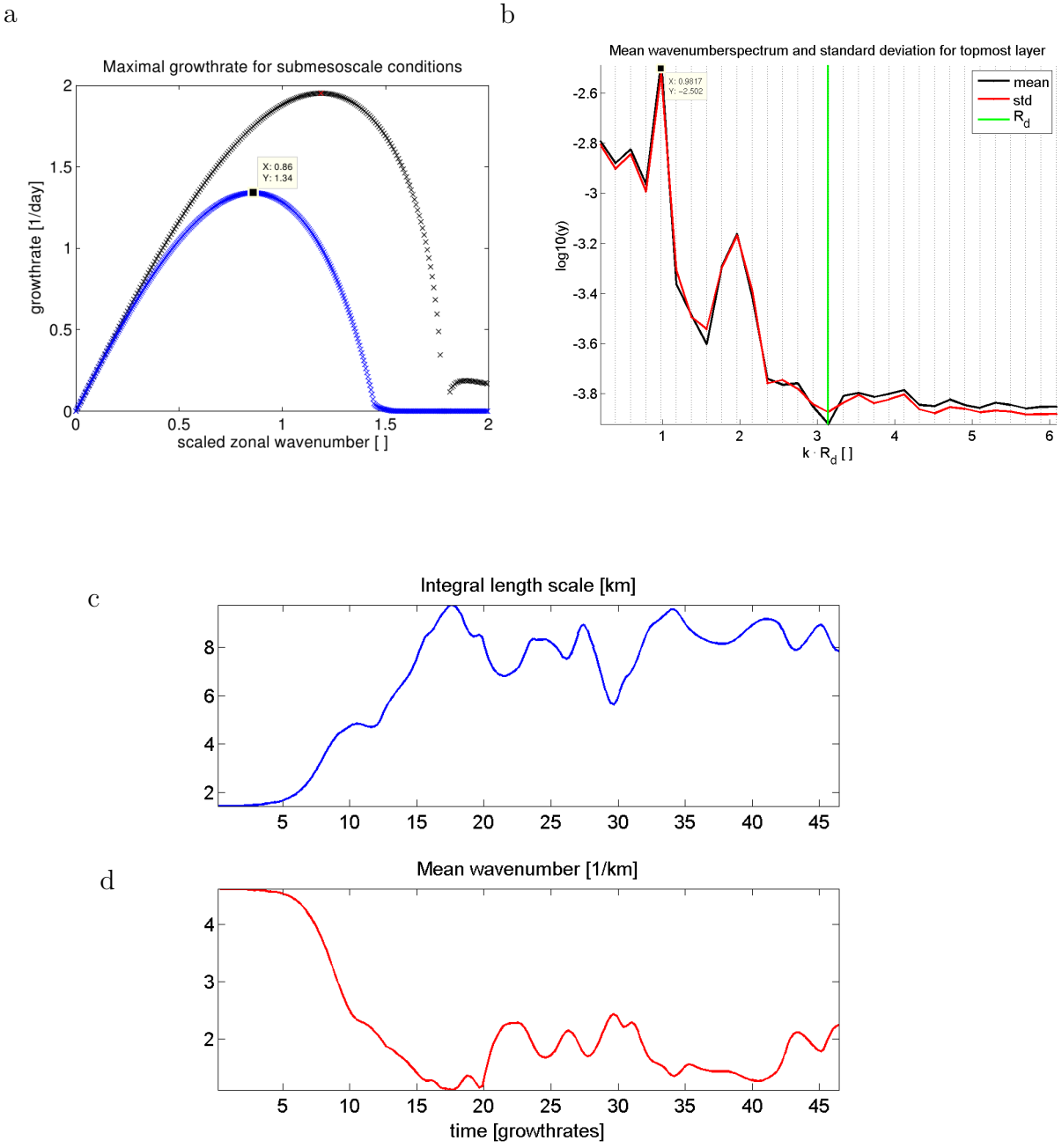

Figure 3.5.: *Submesoscale: (a) Growthrate in scaled wavenumberspace, resulting from a linear stability analysis. The black curve shows the inviscid growth rate, while the blue curve represents the growth rate predicted for the simulation with friction. (b) Wavenumber spectrum of KE for initial linear phase (c) Integral length scale and mean wavenumber (d)*

instability process, at different sections. This problem occurs also in the mesoscale regime and is illustrated and discussed in detail in figure 3.6 (b). Due to the high standard deviation of the KE wavenumber spectrum the calculated length scales are not reliable and therefore additionally the integral length scale and the mean wavenumber are shown in figure 3.5 (c). They are calculated as follows and defined by *Olbers et al.* (2012).

$$L = \frac{3 \cdot \pi}{4} \frac{\int k^{-1} E(k) dk}{\int E(k) dk} \tag{3.1}$$

$$\overline{k} = \frac{1}{E_0} \int k \cdot E(k) dk, \qquad \text{with } E_0 = \int E(k) dk. \tag{3.2}$$

The integral length scale (L) starts with values around 1.8 km, increasing steadily, reaching values of 10 km at the end of the simulation. The same behaviour is observable for the mean wavenumber (compare 3.5 (d)), which is decreasing continuously with time, which is decreasing continuously with time , somewhat fluctuating during the decaying phase staying at small wavenumbers. From this we can assume that an upscale transfer of energy takes place, with growing length scales during the instability process. Though for a more detailed analysis it would be necessary to consider energy fluxes, which is not part of this thesis. The integral length scale and the mean wavenumber are consistent with the results of LSA.

In figure 3.6 (a) the predicted scaled wavenumber (1.2) and next to it in (b) the dominant wavenumber (1.18) of the mesoscale simulation is depicted. The standard deviation (red curve) is as high as in the submesoscale case and exceeds the mean (black) in some points. This can be explained by the fact that the instability process starts at the northern boundary of the domain. Thus calculating the mean of all zonal wavenumber spectra, has a high variance because the waves are already in different phases of the instability process, i.e. some waves have already broken. In figure 3.6 (c) the blue lines show KE of the ten southern most sections, while the red lines are the neighbouring northern sections. The blue lines feature only one wavelength, resulting in only one main peak in the wavenumber spectrum below (d),

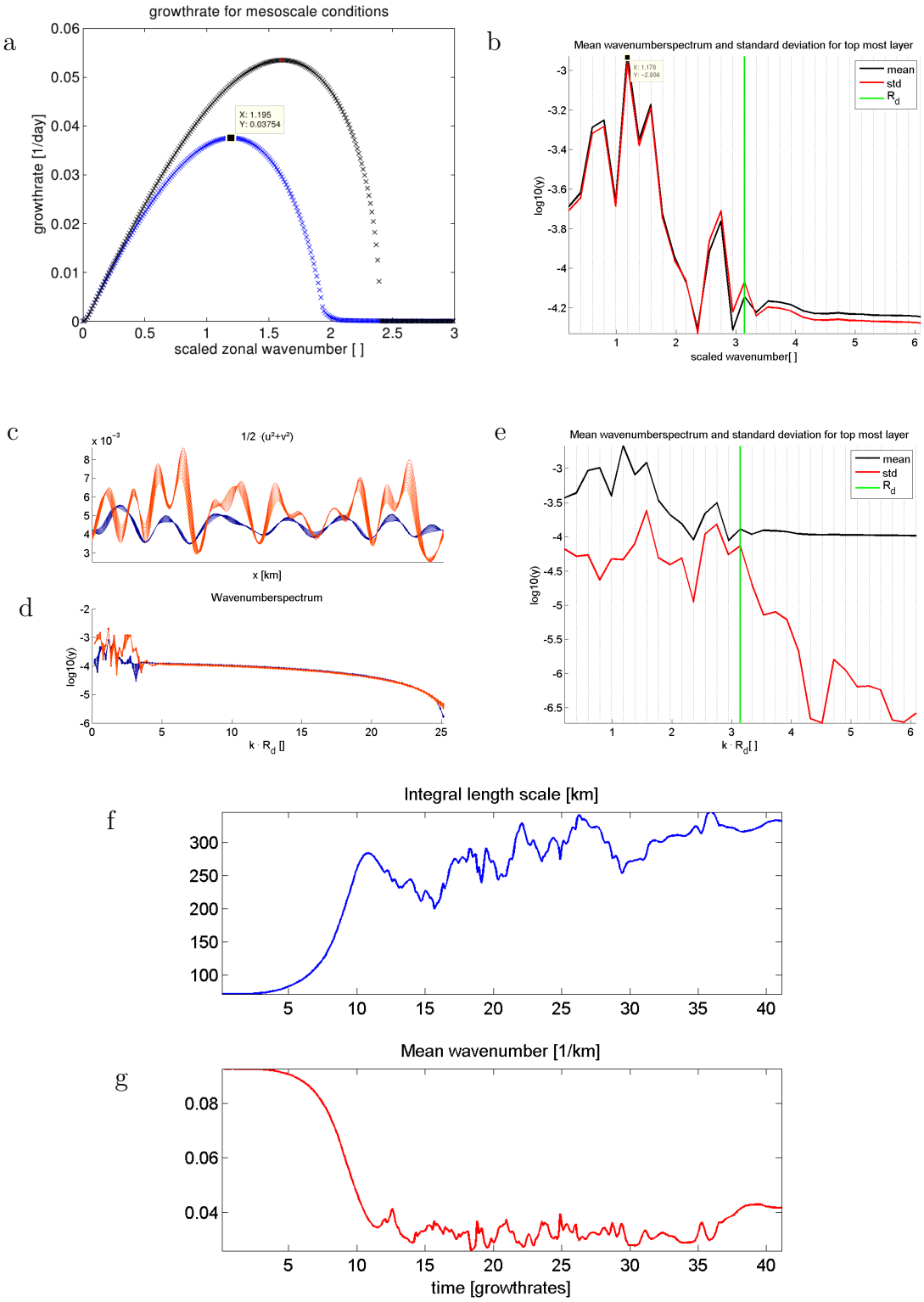

Figure 3.6.: *Mesoscale: (a) Growthrate in scaled wavenumber space, resulting from a linear stability analysis. The black curve shows the inviscid growth rate, while the blue curve represents the growth rate predicted for the simulation with friction. (b) Wavenumber spectrum of KE for initial linear phase. (c) KE for selected along-stream sections and appendant wavenumber spectrum (d). (e) Mean wavenumber spectrum of blue curves in (c). (f) Integral length scale and (g) mean wavenumber*

while for the sections in red already a mixture of different wavelengths is observable. In subfigure (e) the mean wavenumber spectrum of only ten neighbouring sections is shown. The standard deviation is clearly lower, but the dominant wavenumber (1.18) indicates the same, corresponding to a wavelength of 118 km. This matches well with the calculated integral lengthscale in (f), starting with values of 75 km ending up with about 300 km. This development is also observable in figure (g), which depicts the mean wavenumber. The integral length scale and the mean wavenumber are in good agreement with the results of LSA and the dominant wavelength of the wavenumber spectrum of KE.

The same parameters for the intermediate experiment are depicted in figure 3.7. The predicted fastest growing wavenumber is 1.3 (a), well matching the dominant wavenumber in the model run, which is 1.37 (b). Furthermore it stands out that the standard deviation is clearly lower than its mean value. In the intermediate simulation, the instability process arises at all along-stream sections at the same time (which was already observable in the surface temperature fields in figure 3.2 (b)). The main peak in the wavenumber spectrum corresponds with a wavelength of 7.6 km, matching well the initial values of the integral length scale (c), which ends up with values of about 40 km.

In all experiments the predicted length scales are in very good accordance with the actual arising one in the simulations. In the intermediate and mesoscale regime the integral length scale grows strongly during the linear phase (up to 10 growth rates) and continues growing slightly till the end of the simulation. In the submesoscale experiment the integral length scale grows strongly far beyond the linear phase, but does not continue growing afterwards. This might be either due to different growth rates, or due to a limitation by the domain size. The length scales of the mesoscale regime ($\mathcal{O}(100\ km)$) and the submesoscale regime ($\mathcal{O}(1\ km)$) are in accordance with typical eddy sizes associated with this regimes (e.g. *Thomas et al.* (2008)).

From theory ((*Eady*, 1949) and (*Stone*, 1966)) we know, that the fastest growing wave in mesoscale ranges should be $1.6 \cdot L_0$ and slightly below $1.6 \cdot L_0$ in submesoscale ranges (black curves in figure 3.5-3.7 (a)). The values predicted here, are distinctly

a

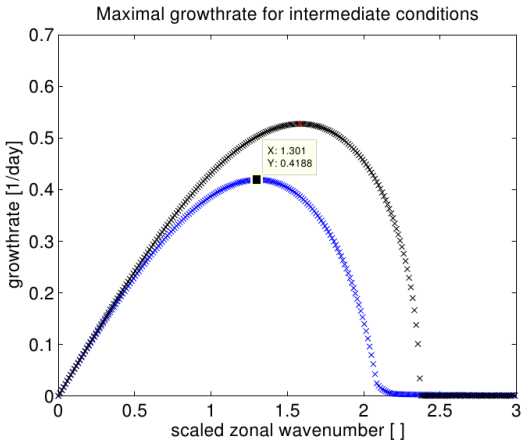

b

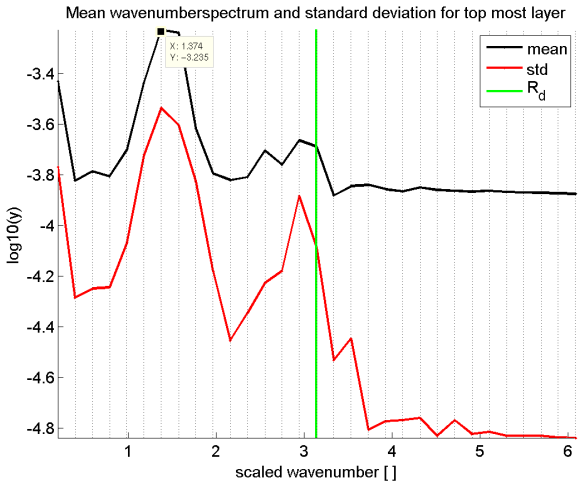

c

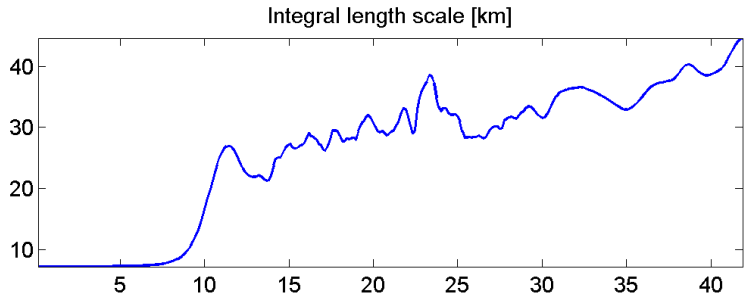

d

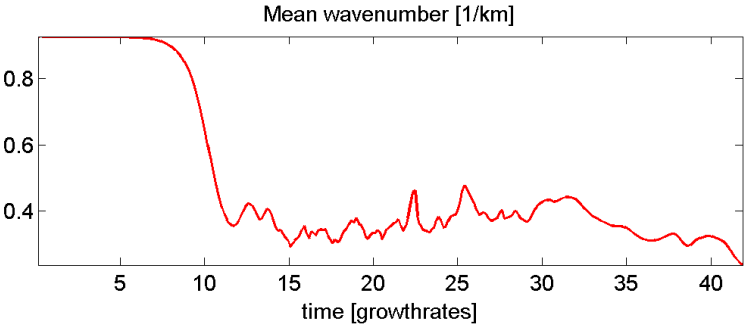

Figure 3.7.: *Intermediate: (a) Growthrate in scaled wavenumberspace, resulting from a linear stability analysis. The black curve shows the inviscid growth rate, while the blue curve represents the growth rate predicted for the simulation with friction. (b) Wavenumber spectrum of KE for initial linear phase. (c) Integral length scale and mean wavenumber (d)*

lower (blue curves in figure 3.5-3.7 (a)). The reason for this is that the referred theory is inviscid, while friction is applied in the simulation. Normally friction should be chosen such that only length scales smaller than the fastest growing one are influenced, which was not possible due to stability reasons of the numerical simulations. Stability could be achieved also with a higher resolution, implying a smaller time step, which has not been realised, due to time-consuming simulations. In all three simulations a second peak in the wavenumber spectrum is visible. This peak is located near the scale of the Rossby radius. This second peak might be the ageostrophic mode described by *Stone* (1970).

In figure 3.8 (a, c, e, g) the structure of perturbation velocity and buoyancy is shown for submesoscale background conditions. The horizontal velocity components have between four and five maxima and minima at the surface and eastward shifted by 90° at the lower boundary. Absolute values are minimal at mid depth. This is more pronounced for the zonal velocity component, while absolute values are higher for the meridional velocity component. The vertical velocity has a maximum of absolute values at mid depth and decreases to the surface and the bottom. A slight intensification towards bottom and surface of absolute values can be recognised for buoyancy, with a minor westward shift of maxima and minima at the bottom. The corresponding parameters of the simulation are from an along-stream section of the southern boundary of the model domain ($\approx 10km$) and shown in figure 3.8 (b, d, f, h). The same structure of intensified absolute values at the bottom and the surface is characterising horizontal velocity and buoyancy, with the same east- and westward shifts in horizontal velocity and buoyancy, respectively. The vertical velocity has maximal values at mid depth, representing the baroclinic structure of the instabilities. In the simulation five minima and maxima show up, which means the predicted wavelength is slightly larger than the one, which is growing fastest in the simulation. The reason is that the predicted fastest growing wave length does not fit in the domain, thus a slightly different wave length is growing in the simulation, which might lead to the difference of simulated and predicted depth-structure.

The results of the LSA and the corresponding parameters of the simulation does

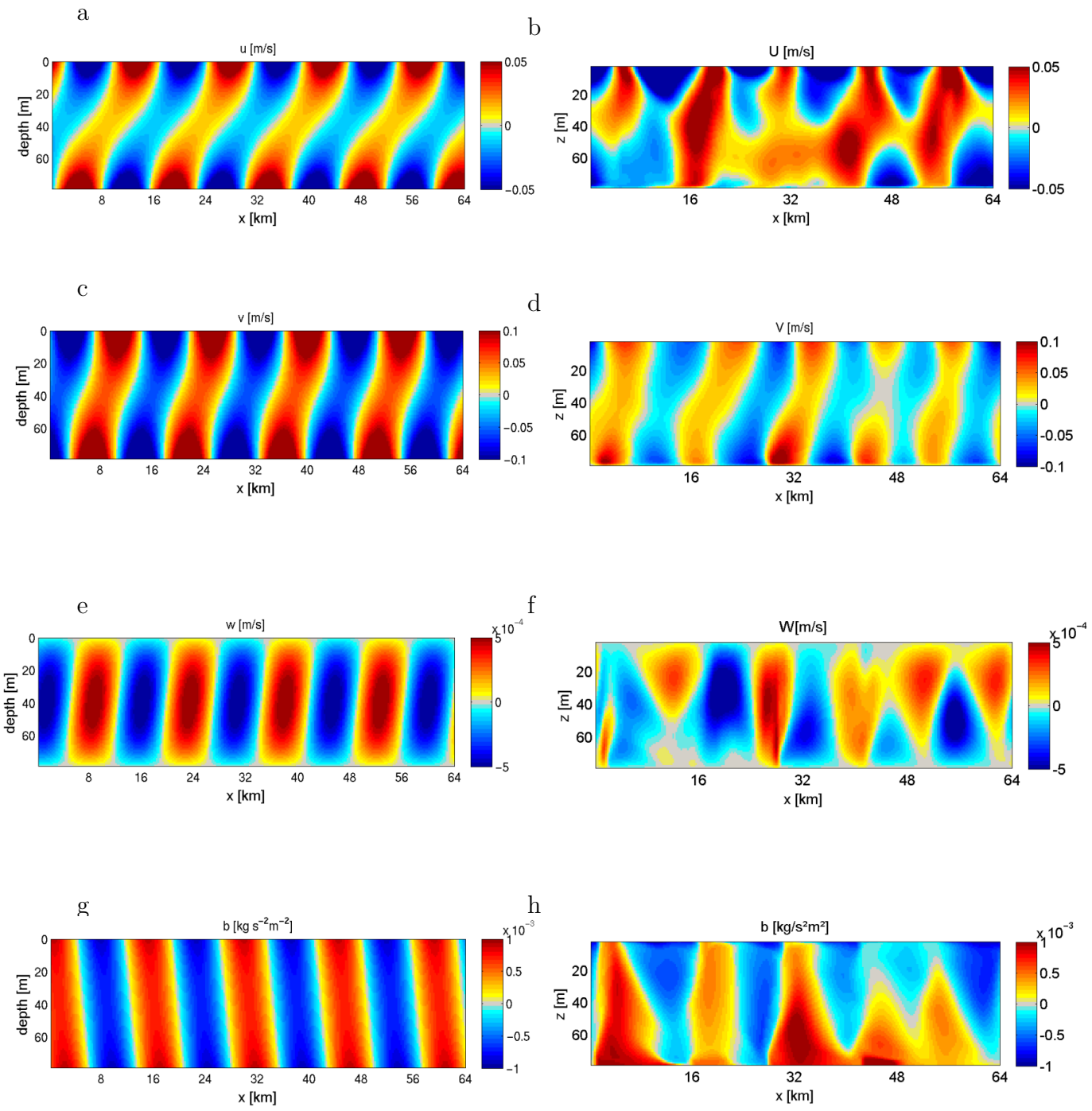

Figure 3.8.: *Submesoscale:Along-stream section of zonal velocity (a,b), meridional velocity (c,d), vertical velocity (e,f) and buoyancy (g,h). For the results of a LSA in (a), (c), (e) and (g) and for the numerical simulation after 10 growth rates from the southern boarder of the model domain in (b), (d), (f) and (h).*

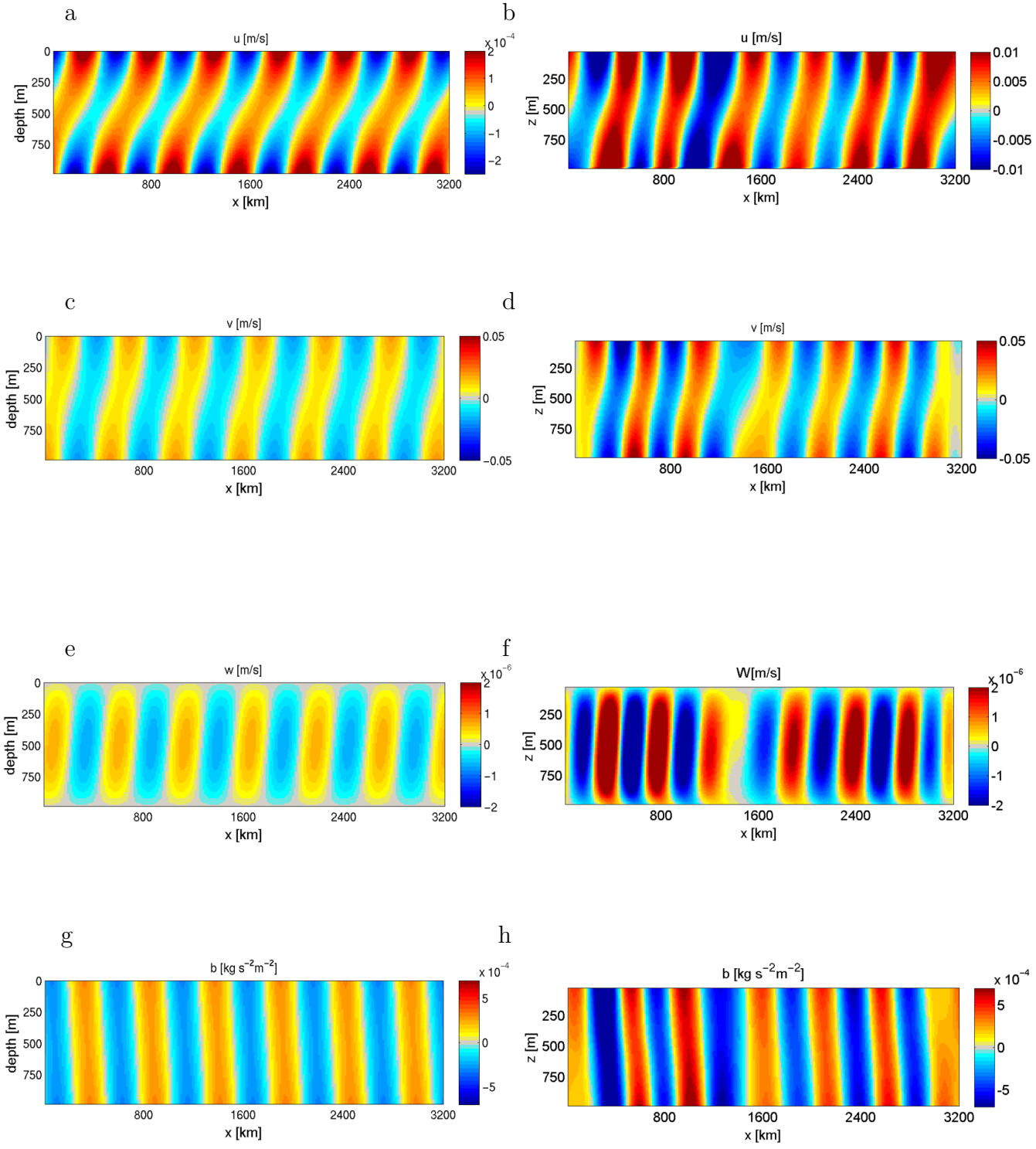

Figure 3.9.: *Mesoscale: Along-stream section of zonal velocity (a,b), meridional velocity (c,d), vertical velocity (e,f) and buoyancy (g,h). For the results of a LSA in (a), (c), (e) and (g) and for the numerical simulation after 10 growth rates from the center of the model domain in (b), (d), (f) and (h).*

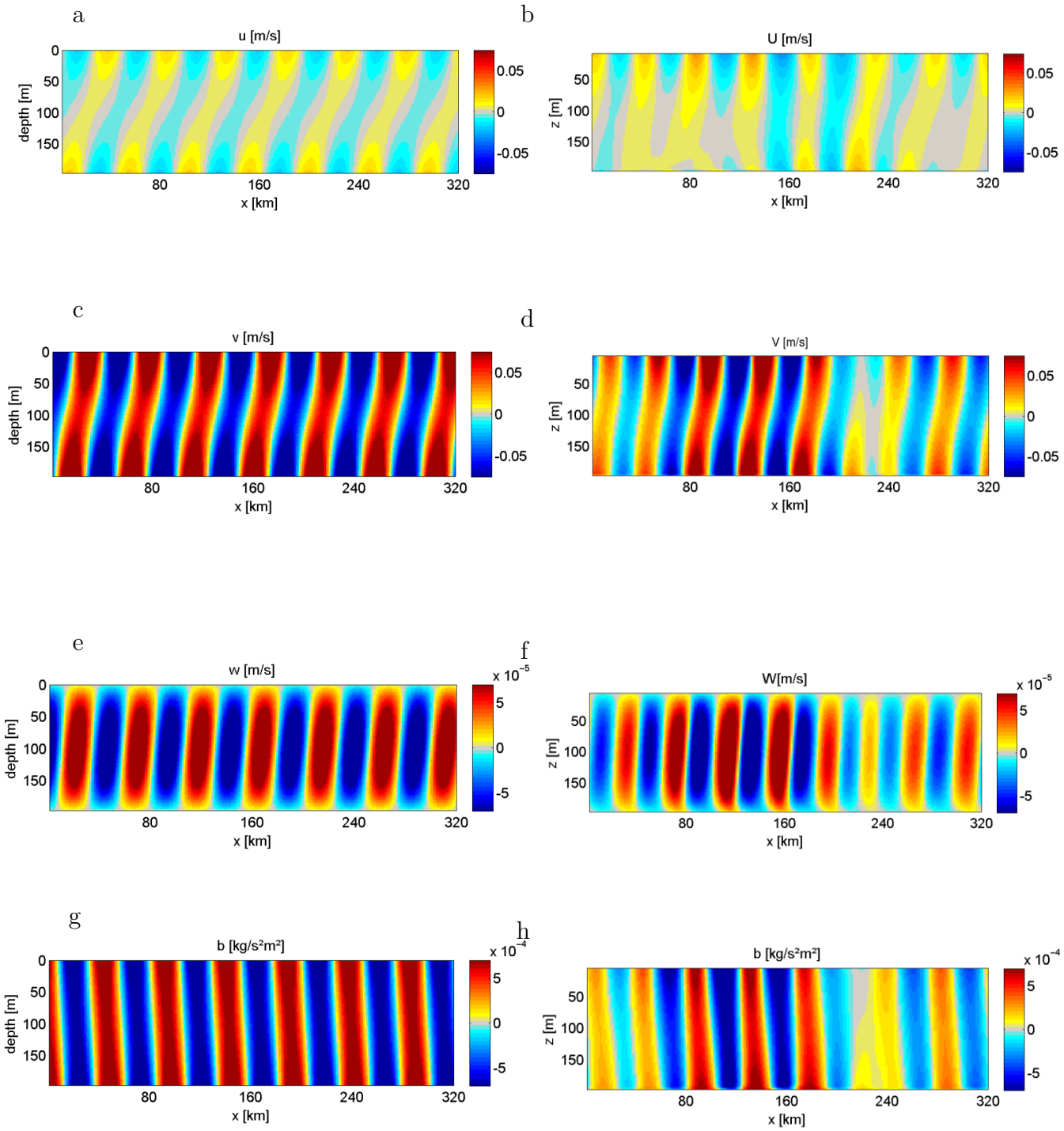

Figure 3.10.: *Intermediate: Along-stream section of zonal velocity (a,b), meridional velocity (c,d), vertical velocity (e,f) and buoyancy (g,h). For the results of a LSA in (a), (c), (e) and (g) and for the numerical simulation after 10 growth rates from the center of the model domain in (b), (d), (f) and (h).*

not match as well, as in the lower resolution runs, or as in the mesoscale and intermediate scale run. This can especially be seen in the simulated buoyancy structure, which is broadest at the bottom and reducing to the surface, while it is constant in LSA.

For the given mesoscale conditions the LSA predicts six maxima and minima perturbations, while the simulation shows 6.5 wavelength (compare figure 3.9). The presented along-stream sections of the simulation are located in the centre of the model domain. The amplitude of the LSA predicted perturbations is about a factor of two lower, except for the zonal velocity, where it is one magnitude smaller. Compared to the submesoscale regime the amplitudes are two orders of magnitude smaller, whereas the total velocity was higher (compare figure 3.16) in the mesoscale simulation.

For the intermediate conditions LSA predicts between seven and eight minima and maxima for the given domain size (compare figure 3.10 (a, c, f *and* g)). Actually seven maxima and minima are developing during the simulation (figure 3.10 (b, d, f *and* h), the presented along-stream sections are located in the centre of the model domain) in u and b perturbations, while eight are growing in v and w perturbations. The structure looks very similar to the predicted ones, though in this case the predicted amplitudes are slightly higher than the realised ones. In the simulation the maxima and minima of u-velocity at the surface are more pronounced than the one at the bottom.

Generally it can be said, that the predicted structure of perturbation velocity and buoyancy are recognisable, but non-satisfying for the submesoscale simulation, while it matches obviously the structures in the intermediate and mesoscale experiments. One possible reason is that the predicted fastest growing wave length does not fit in the domain, thus a slightly different wave length is growing in the simulation, which might lead to the difference of simulated and predicted depth-structure. Only in the submesoscale simulation a different size between maximum and minimum perturbations is observable. The positive perturbations of zonal velocity are narrow at the surface, whereas the negative perturbations are broader, which cannot be predicted

by this linear theory.

3.3. Occurrence of cyclones and anticyclones in the different dynamical regimes

In chapter 1.3 the possibility to define submesoscale and mesoscale conditions by means of the Ri and Ro was described. To verify that all simulations stay in the predefined regimes until the instability process starts, mean, variance and values above (below) a submesoscale $|Ro| = 1$ and $Ri = 10$ are presented in this chapter. Furthermore we can conclude from Ri and Ro whether the system has shifted to a different regime after the instability process. For a quantitative estimate of the occurrence of cyclones and anticyclones distributions of Ro for different depth and time steps are shown, as well as the skewness of the distribution.
To confirm the enhanced gradients and thus the major importance of the advection terms in submesoscale dynamics, ageostrophic and geostrophic flow components are presented separately, as well as time development of the mean balanced mode.
To address the question of different structures in different dynamical regimes, the Okubo- Weiss parameter (OK) is introduced to analyse only the regions defined as eddies. Vertical velocity, pressure perturbation and vorticity are shown, in order to associate characteristic pattern with the eddies.

3.3.1. Rossby and Richardson number

The submesoscale experiments are started with initial conditions of $Ro = Ri = 1$. To verify that the regime stays in submesoscale ranges when the instability process starts figure 3.11 shows the number of all values above a threshold in the entire 3-dimensional domain, given by the absolute value of local $|Ro|$ ($|\zeta/f| \geq 1$) and Ri ($N^2/(\partial u/\partial z)^2 \leq 1$) (figure 3.11 (a)). This values of Ro and Ri where chosen as a threshold consistent with our definition of submesoscale dynamics. Values are normalised by the total number of gridpoints. The difference of global ($\frac{U}{\Omega L}$) and local Ro ($\frac{\zeta}{f}$) is responsible for the initial zero values of Ro. When the instability process starts (compare 3.1) after around 10 growth rates, also the number of gridpoints larger than the threshold Ro increases to values of about 3%, decreasing during the

decaying phase again to 0 %. While the Ri is at submesoscale values at 50 % of all gridpoints in the beginning, decreasing to values of 10 %, after the maximum of the process has passed at about 30 growth rates. Therefor we conclude that the experiment is in a mesoscale range after the instability process is finished.

The local Ro implies also information about the rotational sense. Positive Ro represent positive vorticity and thus cyclones, while a negative Ro implies negative vorticity values and thus anticyclonic motion. Therefor some further calculations are done only for Ro. In figure 3.11 (b) and 3.11 (c) the mean positive and negative Ro with its standard deviation, and the skewness of the distribution of local Ro are shown respectively. The positive mean (maximum is 0.22) exceeds slightly the negative one (maximum is 0.19) and the variance of positive Ro is clearly higher, while the negative standard deviation stays nearly constant. The higher positive variance indicates that more positive extreme values do exist, than negative ones. However no dominance can be determined from negative and positive mean values, since no information about the number of positive and negative Ro is available.

The skewness is regarded to determine a favour for cyclonic or anticyclonic motions and is defined as follows.

The skewness is the 3$^{\text{rd}}$ central moment of a distribution. It is calculated as

$$\frac{\frac{1}{n}\sum_{i=1}^{n}(x_i-\overline{x})^3}{(\frac{1}{n}\sum_{i=1}^{n}(x_i-\overline{x})^{3/2}} \tag{3.3}$$

Zero skewness in the beginning indicates that initially no qualitative difference of cyclonic and anticyclonic motion exists. The skewness increases steeply during the linear phase, which might be an artefact of the adjustment of the unbalanced random pertubation. During the turbulent phase the skewness varies around a value of 1.4 and decreases again to values near zero at the end of the simulation. The skewness is positive during the entire simulation, representing the expected dominance of cyclonic motion.

For the mesoscale simulation only mean (3.12 a) and skewness (3.12 b) of the distribution of Ro are shown, because even at the maximum of the instability process Ro (Ri) above (below) the threshold occur with a commonness of less than 0.001%. The

a

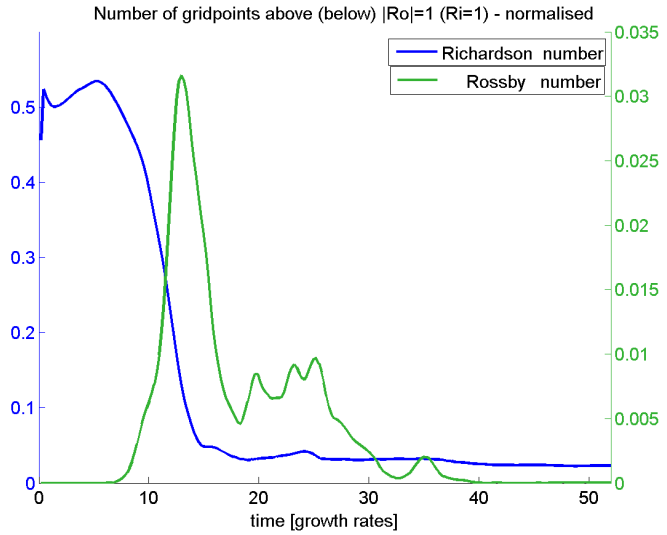

b

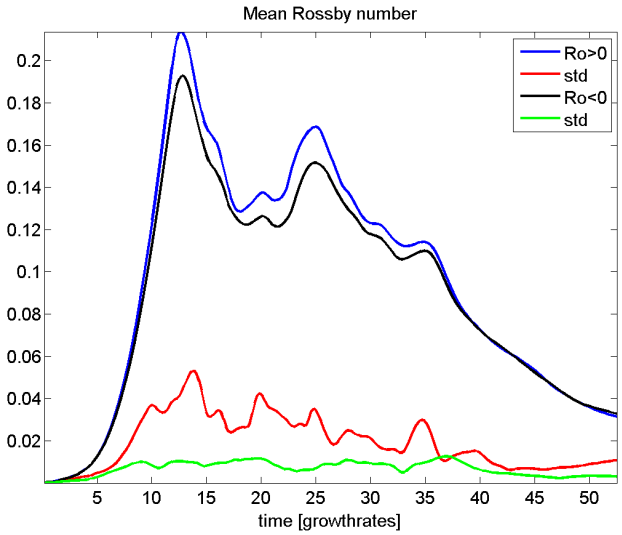

c

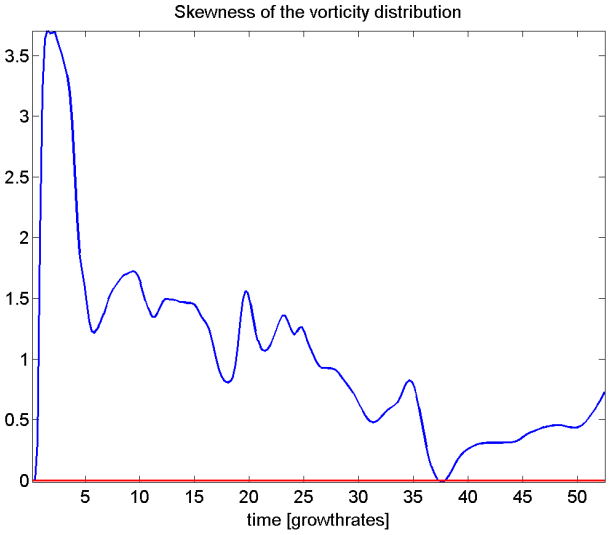

Figure 3.11.: *Submesoscale: (a) Number of gridpoints with values of* $|Ro| \geq 1$ *and* $Ri \leq 1$*, normalised by the total number of gridpoints. (b) Mean positive and negative Ro with its standard deviation. (c) Skewness of the Ro distribution.*

a

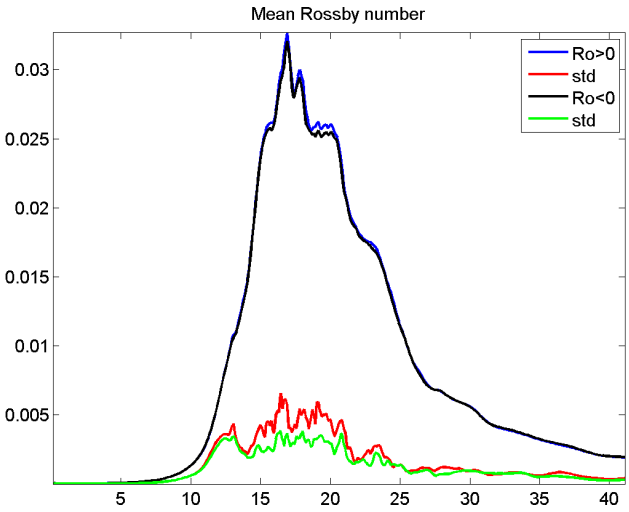

b

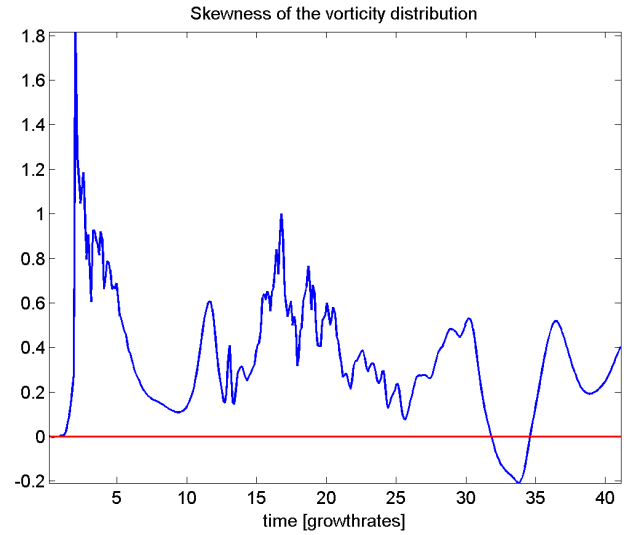

Figure 3.12.: *Mesoscale: (a) Mean positive and negative Ro with its standard deviation. (b) Skewness of the Ro distribution.*

a

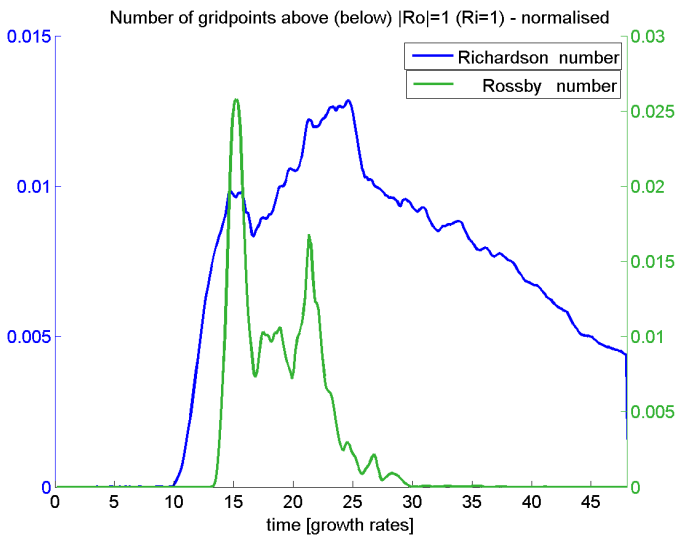

b

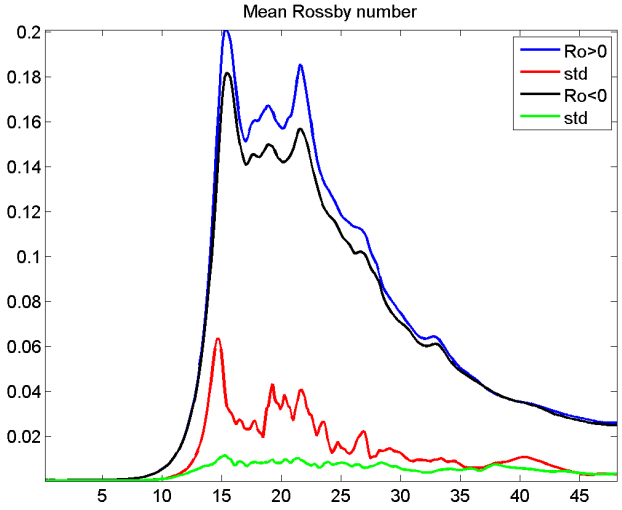

c

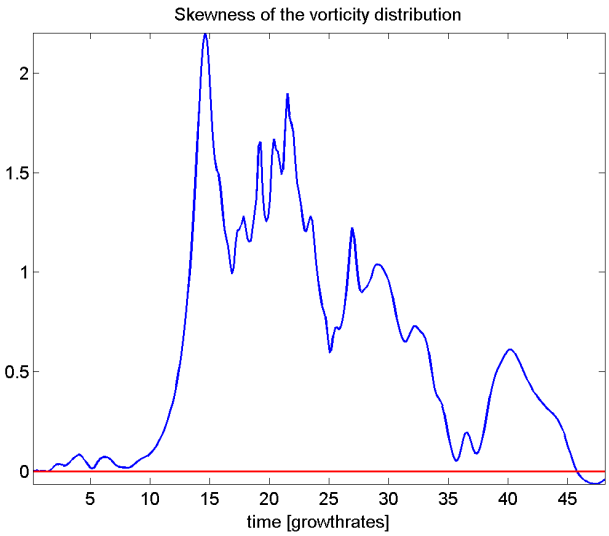

Figure 3.13.: *Intermediate: (a) Number of gridpoints with values of* $|Ro| \geq 1$ *and* $Ri \leq 1$*, normalised by the total number of gridpoints. (b) Mean positive and negative Ro with its standard deviation. (c) Skewness of the Ro distribution.*

positive and negative mean of the Ro distribution show nearly the same form with maximal values one magnitude lower than in the submesoscale experiment (positive: 0.03, negative: -0.03). In contrast to the submesoscale simulation, the variance of the positive mean resembles the negative one. The skewness behaves the same as in the submesoscale case but with distinct lower values (about a factor of four). Opposed to the submesoscale regime, the skewness becomes negative at the end of the simulation.

The same curves can be seen for the intermediate experiment in figure 3.13. The number of values above the threshold Ro (figure 3.13 (a)) makes up 2.5%. For the Ri the values reach about 1.2%, while in the submesoscale case still 20% are below the threshold Ri. The positive and negative mean of Ro lies around 0.2, with a slightly higher positive mean and a higher variance than for negative Ro. The skewness of the distribution of Ro is positive during the entire instability process and becomes negative only for the last few timesteps. The skewness features values of the same range as in the submesoscale simulation. The unexpected high skewness values during the linear phase, as in the submeso- and mesoscale simulation, are not observable here.

Furthermore in figure 3.14 the distribution of local Ro in the submesoscale simulation can be seen for different time steps and depth layers. A bootstrapping method was applied to identify mean and standard deviation of the distribution of local Rossby numbers. The procedure is to equate each data point with a number produced by a random number generator between zero and one. All values above the median of all random numbers are taken to be one of the samples we need to make up our bootstrap data set. Afterwards the distribution is calculated. This procedure was applied 100 times, and from all distributions the mean distribution and its standard deviation are calculated.

The black lines are the calculated mean from the random samples, the coloured lines gives the standard deviation for each mean. After seven growth rates (a) the distribution is still almost symmetric, only for the topmost layer a slight dominance of positive values is observable. After 13 growth rates (b) the skewness of the distri-

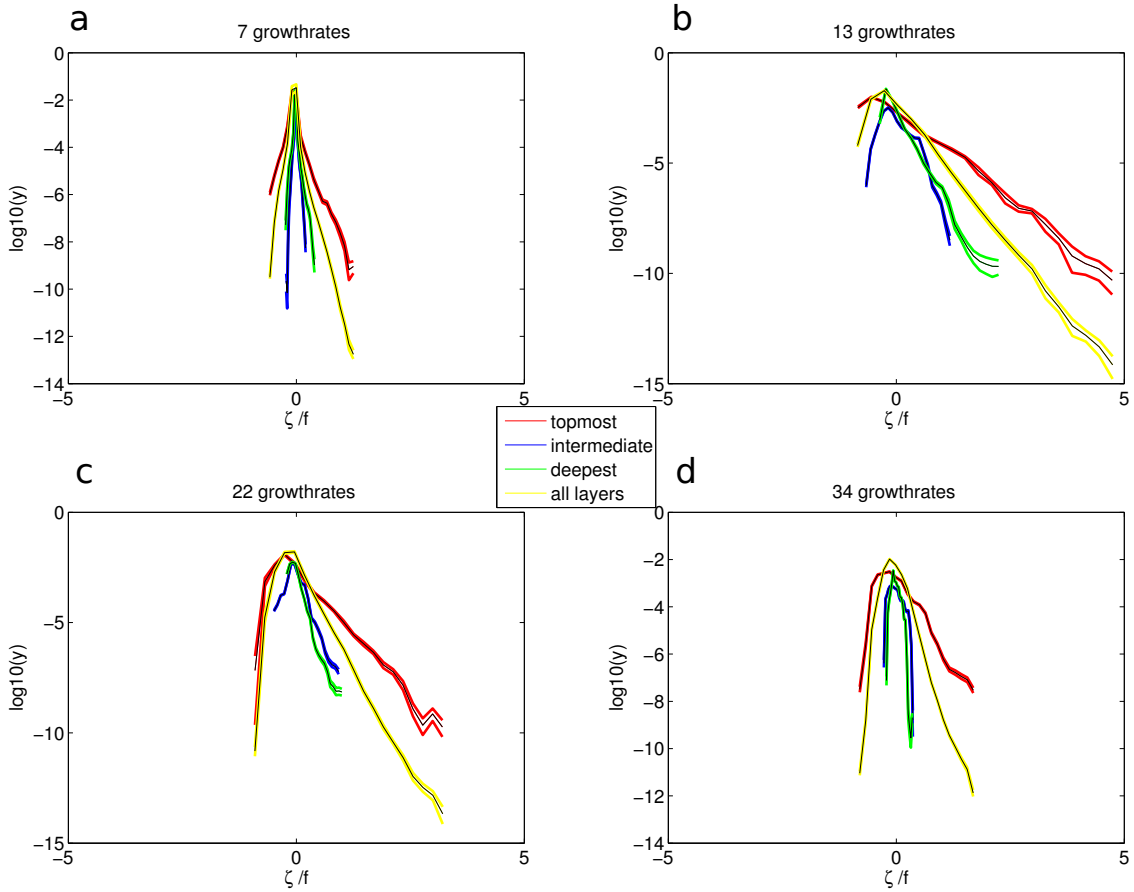

Figure 3.14.: *Submesoscale simulation: Distribution of Ro* ($\frac{\zeta}{f}$) *for different stages of the process and for different layers. (a) - initial linear phase, (b) and (c)- turbulent process and (d) - decaying phase. The black line is the respective mean of the distribution of the topmost layer (red), the intermediate layer (blue), the deepest layer (green) and of all layers (yellow), the colored lines give the standard deviation.*

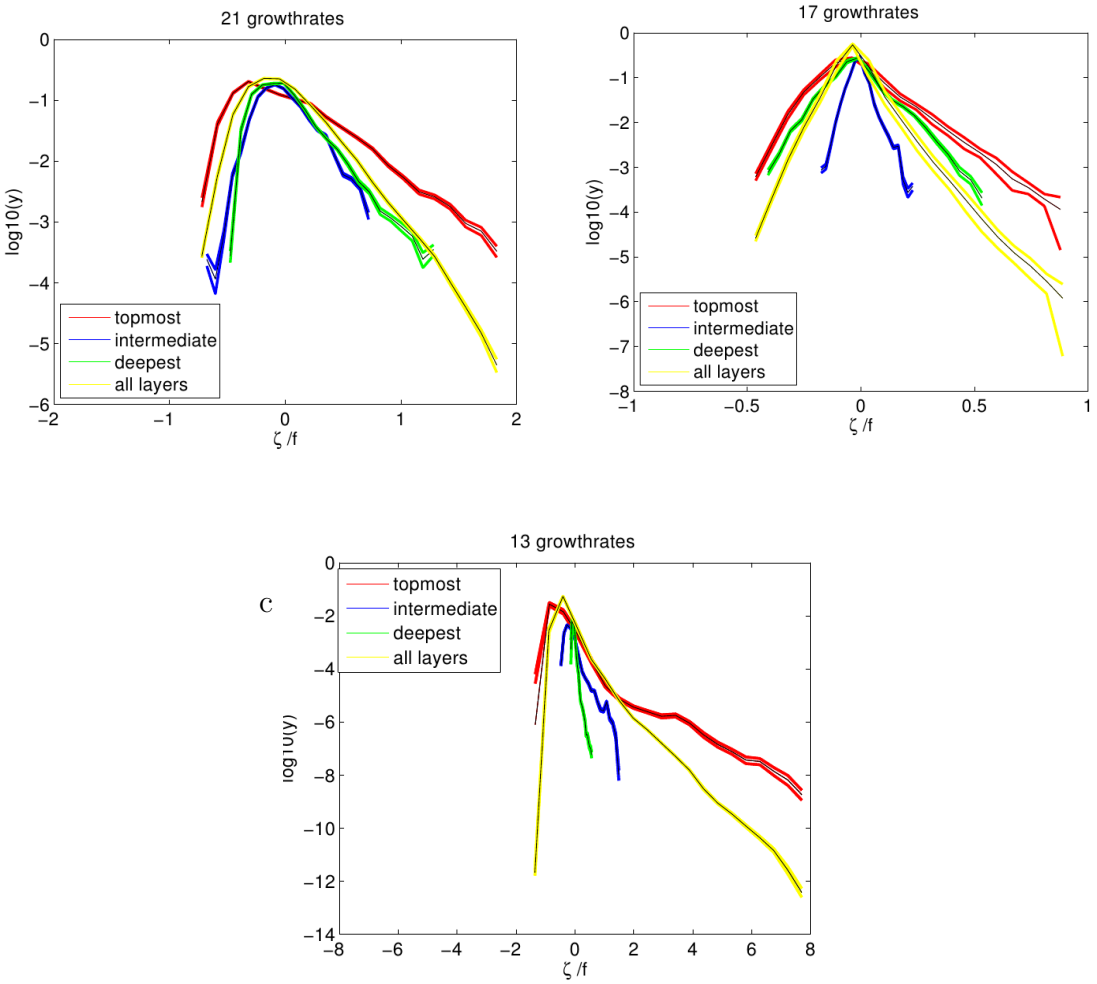

Figure 3.15.: Distribution of Ro ($\frac{\zeta}{f}$) for different layers. (a) Intermediate simulation, (b) mesoscale simulation, (c) submesoscale with nonlinear buoyancy gradient (experiment 1 in table 2.3), all representing the turbulent phase. The black line is the respective mean of the distribution of the topmost layer (red), the intermediate layer (blue), the deepest layer (green) and of all layers (yellow), the colored lines give the standard deviation.

bution is clearly visible, with positive values up to $Ro = 5$, while negative values do not undercut -1 by much. From equation 1.7 we know that negative values should not fall below -1, this lower boundary for Ro is clearly visible here, while positive Ro can develop freely. However locally negative Ro might undercut this value, as it happenend in the lower resolution simulations (not shown). Equation 1.7 assumes conservation of EPV, which is not completely fullfilled in the presented simulations due to friction (development of EPV is not shown). In addition the thermal wind equation is used to derive equation 1.7, which might be not completely valid for submesoscale regimes.

Furthermore a surface intensification of the skewness of the distributions can be recognised. The topmost layer (red curve) has distinct higher positive values, than the intermediate (blue) and the deepest layer (green), while the distributions are nearly equal for negative Ro. After 22 growth rates (c) the positive Ro values are decreasing, coming again to a nearly symmetric distribution after 34 growth rates (d). The maximum of the distribution of the surface layer is shifted from zero towards slight negative values after the linear phase ended. It means in effect, that more slightly negative Ro than positive Ro exist.

The reader can find the mesoscale distributions during the turbulent phase in figure 3.15 (b). Inherently, the range of Ro is here completely different. Both, negative and positive Ro do not exceed absolute values of one. Nevertheless a slight skewness during the turbulent phase of the instability process towards positive values is observable. The reason is that Ro approaches values of one, which implies that per definition submesoscale dynamics (chapter 1.3) occur here, leading to the observed slight skewness. Again a depth dependency is recognisable, while it is in this case intensified towards surface and bottom, where as the intermediate layers have lowest values. This structure corresponds well with the LSA predicted minimum perturbation velocity values at mid depth.

The distribution of Ro for the intermediate simulation can be seen in figure 3.15 (a). Again a surface intensification of the skewness of the distribution is visible. At the maximum of the instability process (after 21 growth rates; figure 3.15 (a)) the

positive Ro reaches values of 2, while negative values do not undercut $Ro = -1$. In figure 3.15 (c) the distribution of Ro for the submesoscale experiment with the non-linear buoyancy gradient is presented (experiment 1 in table 2.3). The positive Ro reaches distinct higher values than in the submesoscale experiment with a linear buoyancy gradient. As already mentioned in the introduction, the non-linear structure represents the conditions of a ML, with its sharpened gradients better. Thus we can expect an even higher asymmetry between cyclones and anticyclones than mainly presented here, by the linear submesoscale experiment.

Summing up the analysis of the dimensionless numbers, all simulations remain in their initial regimes at least during the instability process. At the end of the simulation the submesoscale and intermediate run feature mesoscale characteristic with low (high) Ro (Ri), which strengthen the suggestion of the previous section, that an upscale transport of energy towards larger scales take place. The intermediate simulation resembles the submesoscale run more closely, with nearly as high mean values, but less extrem values.

We can determine a dominance of positive Ro for the submesoscale experiments, representing the expected cyclonic favor of this regime, while only a slight asymmetry is visible in the mesoscale simulation. The intermediate case stays in between, with a slight dominance of positive Ro. Even if positive Ro do not reach values of 1 (as it is the case in the mesoscale simulation, or at the end of the submesoscale run) a skewness towards positive Ro is observable, which means the lower boundary given through equation 1.7 cannot be the only reason for a cyclonic dominance.

3.3.2. Geostrophic and ageostrophic flow components

To quantify the importances of the individual terms of the equations of motion in the different dynamical regimes this section depicts surface patterns of ageostrophic and geostrophic flow components separately, as well as time development of the mean balanced mode and the relation between mean geostrophic and ageostrophic KE.

The total geostrophic flow component ($\boldsymbol{u}_{\text{geo}}$) is the sum of the geostrophically balanced background flow ($\boldsymbol{u}_{\text{back}}$) and the geostrophic part of the perturbation ($\boldsymbol{u}'_{\text{geo}}$), $\boldsymbol{u}_{\text{geo}} = \boldsymbol{u}'_{\text{geo}} + \boldsymbol{u}_{\text{back}}$.
$\boldsymbol{u}'_{\text{geo}}$ is calculated as:

$$\boldsymbol{u}'_{\text{geo}} = \frac{-1}{f\rho_0} \cdot \nabla_h p' \tag{3.4}$$

The subscripted h denotes the horizontal component and p' the perturbation pressure. The ageostrophic component is then defined as $\boldsymbol{u_{ageo}} = \boldsymbol{u'} - \boldsymbol{u_{geo}}$.
In figure 3.16 the geostrophically balanced and ageostrophic velocity components are illustrated after 15 growth rates (a-c) and after 25 growth rates (d,e). The enhanced geostrophic and ageostrophic velocities occur at the same regions where the spiral eddies are located. The ageostrophic velocity (b) is a factor of two lower than the geostrophic component (a). The ageostrophic velocity seems to rotate predominantly anticyclonic, as seen in figure 3.16 (e) and even better visible in the intermediate experiment 3.18 (b).
In order to exclude that the ageostrophic velocity is always anticyclonic the ageostrophic relative vorticity is shown in the Appendix (figure A.2 (a)), which features cyclonic and anticyclonic regions.

Divergence equation

$$\frac{D}{Dt}\left(\frac{\partial u}{\partial x} + \frac{\partial v}{\partial y}\right) - f\zeta_{\text{ageo}} = Ah\left(\frac{\partial^2}{\partial x^2} + \frac{\partial^2}{\partial y^2}\right)\frac{\partial w}{\partial z} + Av\frac{\partial^3 w}{\partial z^3} \tag{3.5}$$

Ah and Av are the horizontal and vertical viscosities.
To determine which term of equation 3.5 is dominating the ageostrophic relative vorticity (ζ_{ageo}) the Coriolis term and the friction term (figure A.2 (b)) are calculated separately. The difference between the latter both is then defined as the residuum (tendency and advection terms together (figure A.2 (c)). ζ_{ageo} is of the same order as the residuum, whereas friction features slightly lower values. In the centre of the spirals however the friction is enhanced and thus also influencing ζ_{ageo}. Friction always acts against the total velocity. Thus the friction might partly explain, why

ζ_{ageo} is anticyclonic in the cyclonic spirals. But further investigation would be necessary to determine the dependence of ζ_{ageo} to the tendency, the advection and the friction terms.

In subfigure (c) the geostrophic velocity is shown underlayed by the pressure perturbation. One equal sized high and low pressure system is observable, as well as six further, but distinct smaller, low pressure systems. The magnitude of the pressure anomalies is the same for positive and negative systems, but the size is different. This points the dominance of cyclonic low pressure systems out again, as well as the different sizes of cyclones and anticyclones, postulated by the theory introduced in chapter 1.3. In anticyclonic regions no enhanced ageostrophic velocity is visible. The ageostrophic component acts mainly against the geostrophic one, leading to lower total velocities compared to geostrophic ones.

The geostrophic velocity of the mesoscale simulation (figure 3.17 (a)) reaches values of 1.4 ms^{-1} and follows mainly three low pressure systems, two large and one small high pressure system (3.17 (b)). The structure of enhanced ageostrophic velocity (3.17 (c)) is not that clearly associated with eddy regions, as in the submesoscale experiment. The ageostrophic velocity reaches maximal values of 0.3 ms^{-1}.

In the intermediate simulation geostrophic velocity (figure 3.18 (a) does not exceed 1.2 ms^{-1}. At this point of time three low and one high pressure systems of equal size have evolved (compare figure 3.18 (b)). The structure of the ageostrophic velocity in (c) is like in the submesoscale case associated with the eddies. The maximal ageostrophic velocity slightly exceeds values of 0.3 ms^{-1}.

In all three regimes the ageostrophic velocity reaches the same maximal values of 0.3 ms^{-1} – only the pattern differs – while the geostrophic and total velocity (the latter is not shown here) differs about a factor of four between the mesoscale and the submesoscale regime and a factor of three between intermediate and submesoscale dynamics. From this it follows that the relation between geostrophic and ageostrophic flow components is different in the particular experiments. This reveals the following relation between geostrophic and ageostrophic components in the submesoscale, intermediate and mesoscale regime (1:1/3:1/4). To quantify this

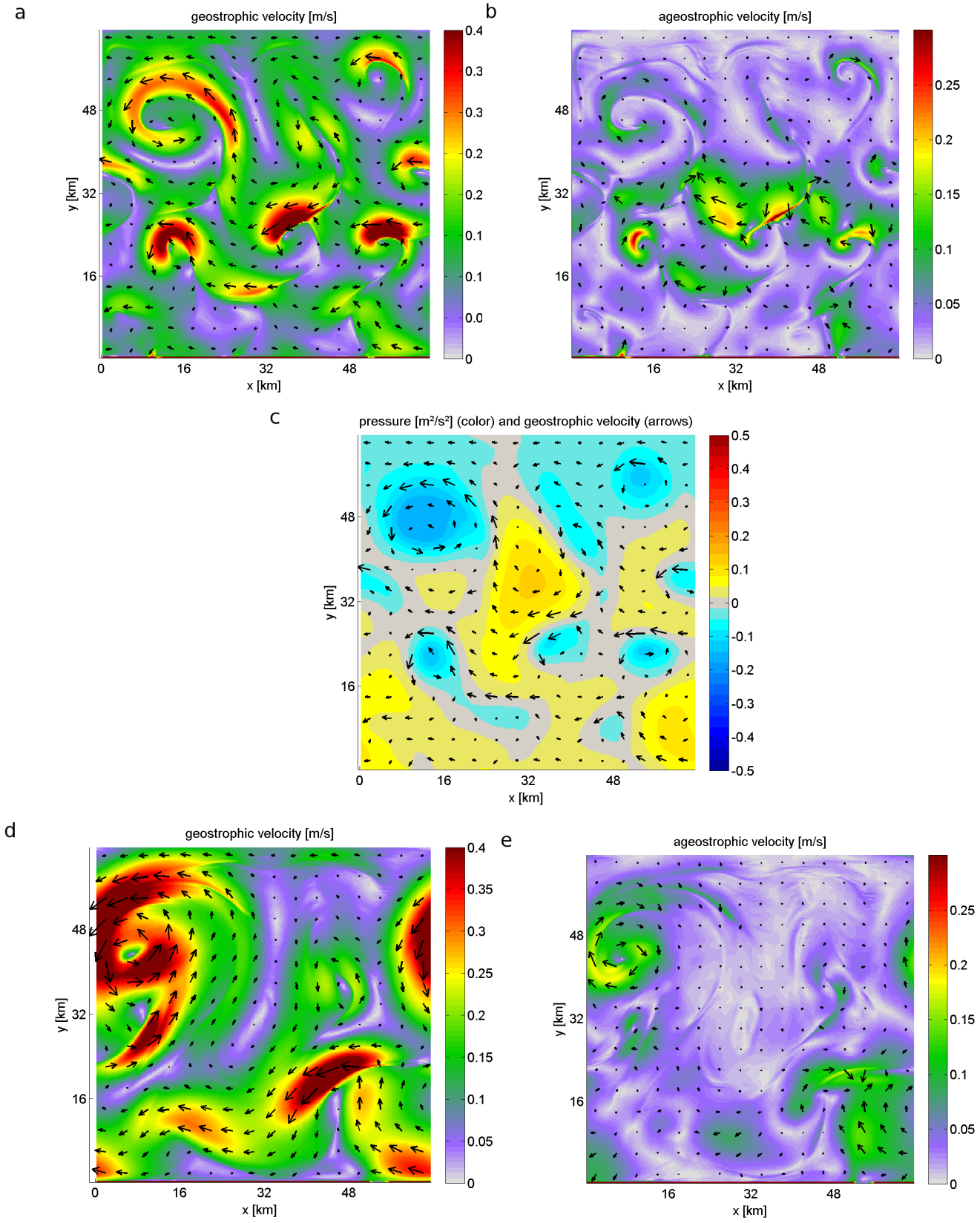

Figure 3.16.: *Submesoscale: Velocity components after 15 (a,b and c) and after 25 growth rates (d and e) at the surface. Geostrophic velocity (a and d), ageostrophic velocity (b and e) and pressure anomaly with overlayed geostrophic velocity (c)*

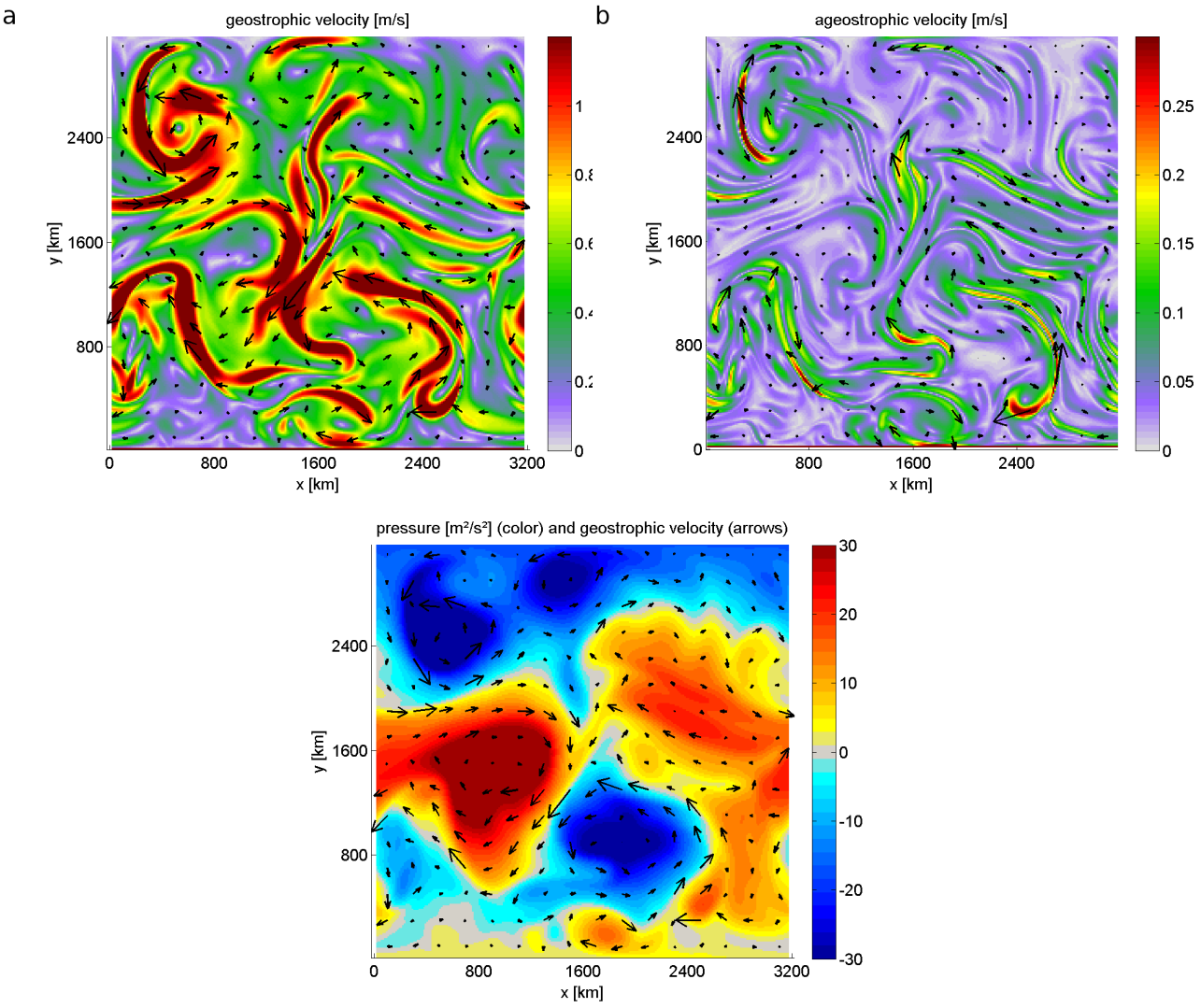

Figure 3.17.: *Mesoscale: Velocity components after 19 growth rates at the surface. Geostrophic velocity (a), ageostrophic velocity (b) and pressure anomaly with overlayed geostrophic velocity (c)*

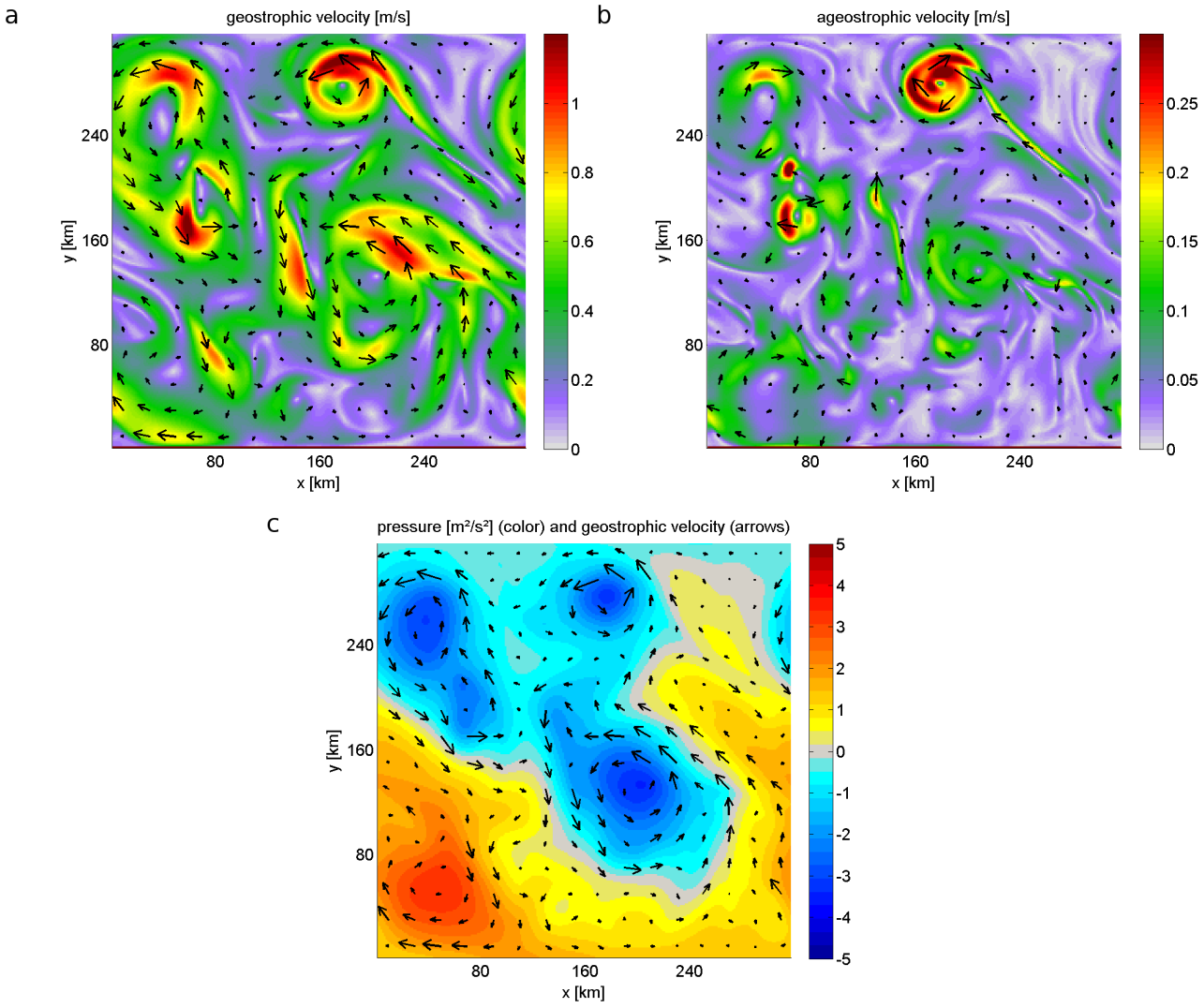

Figure 3.18.: *Intermediate: Velocity components after 21 growth rates at the surface. (a) Geostrophic velocity, (b) ageostrophic velocity and (c) pressure anomaly with overlayed geostrophic velocity*

relation the time dependent importance of ageostrophic versus geostrophic motion, the relation of ageostrophic KE to geostrophic KE and the mean balanced mode are shown in figure 3.19.

The balanced mode (ϵ_{bal}) indicates the relative importance of geostrophic and ageostrophic motions (*Capet et al.*, 2008). If ϵ_{bal} is 0, the flow is totally geostrophic, while $\epsilon_{bal} \approx 1$ is associated with an highly unbalanced flow field.

$$\epsilon_{\mathrm{bal}} = \frac{|\nabla \cdot (\boldsymbol{u_H} \cdot \nabla_H \boldsymbol{u_H}) - f\zeta + \frac{1}{\rho_0}\nabla_H^2 p|}{|\nabla \cdot (\boldsymbol{u_H} \cdot \nabla_H \boldsymbol{u_H})| + f|\zeta| + |\frac{1}{\rho_0}\nabla_H^2 p| + f\zeta_{\mathrm{rms}} + |\frac{1}{\rho_0}\nabla_H^2 p|} \tag{3.6}$$

Where $\boldsymbol{u_H}$ denotes the horizontal velocity components, ζ the vertical component of relative vorticity, ∇_H the horizontal gradients, ρ the density, f the Coriolis parameter and p the pressure.

The relation between ageostrophic and geostrophic KE in the submesoscale regime reaches a maximum of 0.15 (figure 3.19 (a)), while in the intermediate case (e) the relation does not exceed 0.05 and in the mesoscale regime values of 0.005 (c). This looks very similar for the balanced mode calculation. The maximal submesoscale value (b) here is 0.2, 0.02 in the intermediate simulation (f) and 0.015 in the mesoscale run (d). The balanced mode shows very high values in the beginning in all three simulations, which is probably due to the initially applied random perturbation which is not geostrophically balanced. The balanced mode and the relation between ageostrophic and geostrophic KE reveal the same different importance of the ageostrophic flow component for the different regimes, as the snapshots of surface ageostrophic and geostrophic flow components (figure 3.16-3.18).

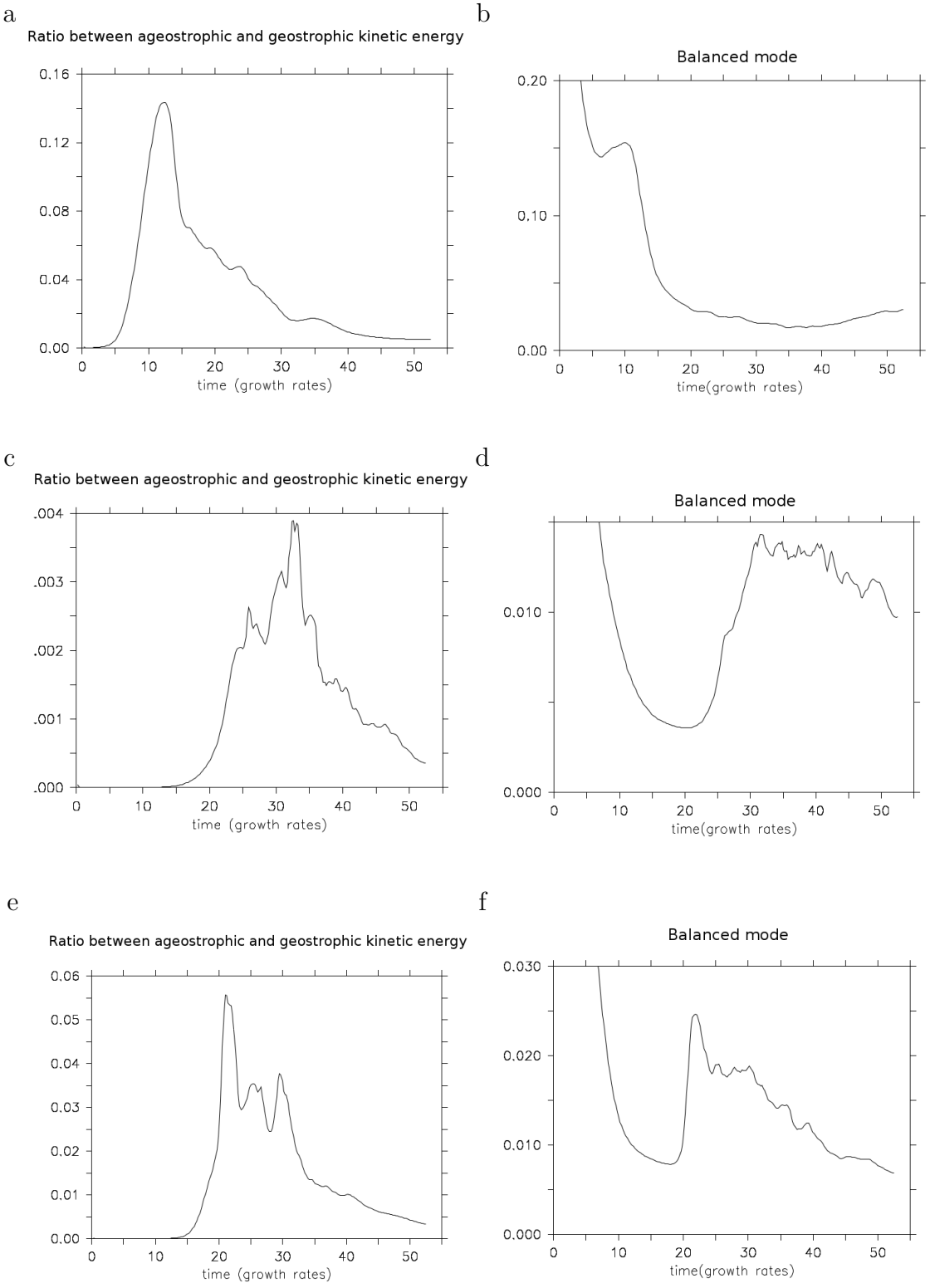

Figure 3.19.: *(a), (c) and (e) Ratio between ageostrophic and geostrophic kinetic energy. (b), (d) and (f) Domain mean of the balanced mode (Skyllingstad and Samelson, 2012). For the submesoscale simulation in (a) and (b), for the mesoscale simulation in (c) and (d) and for the intermediate one in (e) and (f).*

3.3.3. Okubo-Weiss-parameter and eddy structure

The Okubo-Weiss-parameter (OK) is introduced to define eddy regions and is utilised to make a qualitative statement about the eddy structure in the different regimes, as well as about the associated vertical velocity and vorticity.

The OK gives the importances of vorticity versus shear and strain deformation, a vorticity dominated region is an eddy (*Okubo*, 1970). The OK is calculated as:

$$OK = \alpha^2 + h^2 - \zeta^2 \tag{3.7}$$

with $\alpha = \frac{\partial u}{\partial x} - \frac{\partial v}{\partial y}$ (stretching deformation)
with $h = \frac{\partial v}{\partial x} + \frac{\partial u}{\partial y}$ (shearing deformation)
with $\zeta = \frac{\partial v}{\partial x} - \frac{\partial u}{\partial y}$ (relative vorticity)

The mean and the standard deviation for the whole domaine are calculated for each timestep. An eddy is then defined as a region where $OK \leq -0.2std(OK)$ (which is a common definition e.g. *Emelianov et al.* (2004)).

OK is an estimate for two-dimensional flows. We assume it to be still valid for submesoscale regimes, where vertical velocities changes are still one order of magnitude lower than horizontal velocity changes (compare e.g figure 3.20 (e) and 3.21 (a)). Possible problems may occur if the strain rate ($\sqrt{\alpha^2 + h^2}$) is as high as the relative vorticity (ζ) in the same spots. If this is the case the OK will approach values of zero. In order to figure out if this is the case in the submesoscale regime we depict the strain rate and the absolute value of relative vorticity in the Appendix (figure A.1). The comparison reveals that in the tails of the spirals the strain rate and the relative vorticity (ζ) are both large, while in the centre of the spirals only ζ reaches high values. This is also the case in the mesoscale simulation (not shown), with the difference that total values of the strain rate and the vorticity are lower. We conclude from this, that the presented OK might sometimes underestimate the length of the spirals, but can still be used to qualitatively associate vertical velocity and relative vorticity with eddies. The OK of the submesoscale regime is depicted as well as pressure perturbation, vertical velocity and vorticity in the regions defined as eddies by the OK after 12 growth rates (figure 3.20 (a,b)) and after 15 growth rates (c-f).

Figure 3.20 (a) and (c) show the OK normalised by $0.2 \cdot std(OK)$, the blue regions indicate vorticity dominated areas, hence eddies, while red values represent strain and shear dominated areas. The darker the blue the more intensive is the eddy. Already in the first shown figure, (3.20 *a*) a difference in the structure of cyclonic and anticyclonic eddies can be recognised. While positive vorticity occurs in small, filamentlike regions, but very intense, the structure of negative vorticity values is more expanded but with lower absolute values. Adjecent to cyclonic regions always a region of high shear dominance can be found (positive OK values). We like to draw attention also to the smaller size of cyclonic eddies, compared to anticyclones, in the initial phase (3.20 (b)). After 15 growth rates the cyclonic filaments are rolled into a spiral, while anticyclones show a closed circulation pattern (compare figure 3.20 c and d). The anticyclones are still larger at this stage, but associated with obvious weaker vorticity values (d).

Mostly vertical downward velocities are associated with the spiral eddies, while the anticyclonic eddies have low absolute values of vertical velocities in the centre (figure 3.20 e). The positive and negative pressure perturbations in (f) have similar amplitudes, but differ in their size.

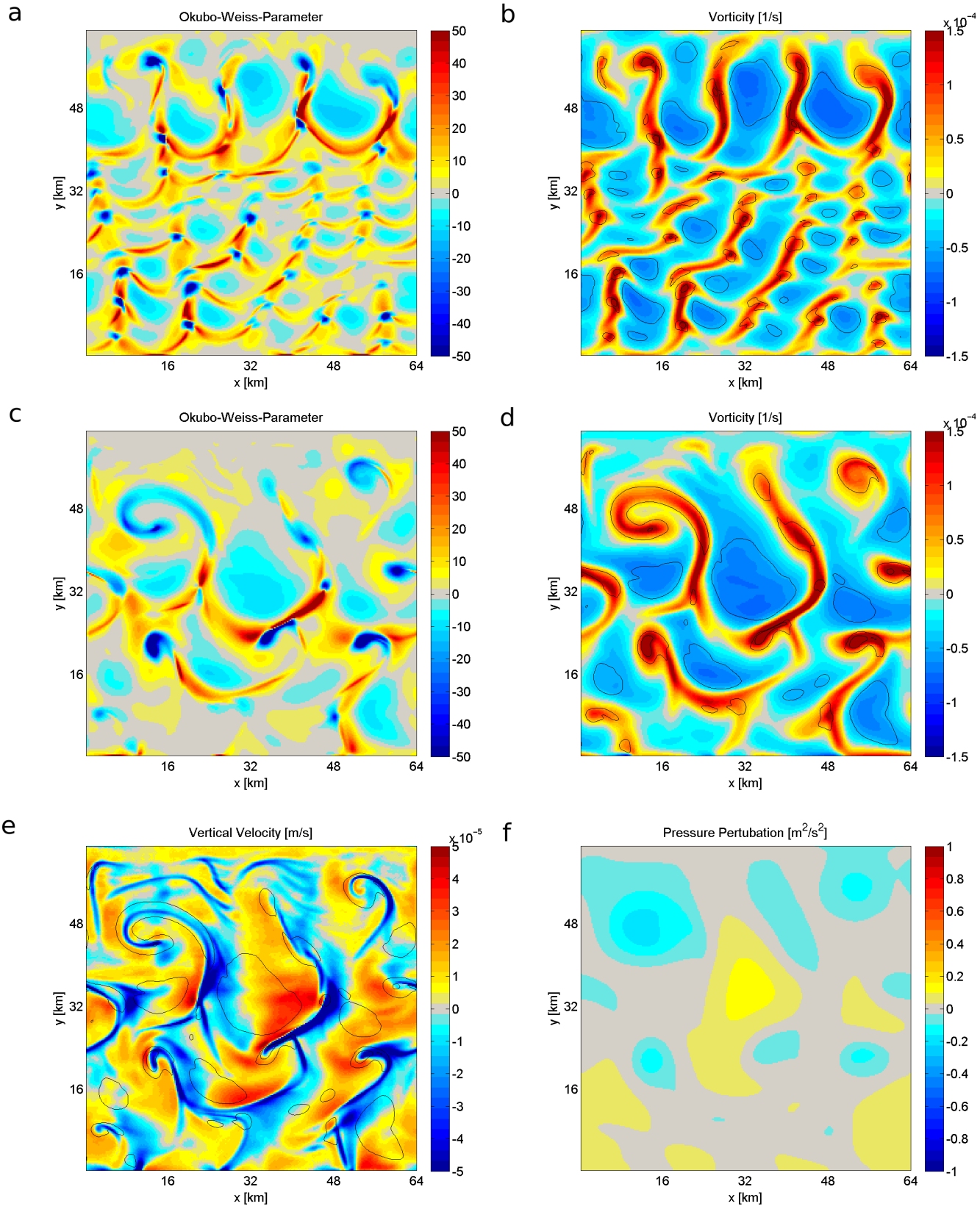

Figure 3.20.: *Submesoscale: OK (a) and relative vorticity (b) with contours of eddies, defined by OK after 10 growth rates at the surface, (c) and (d) the same as (a) and (b) but after 15 growth rates, pressure pertubation (e) and vertical velocity (f) with contours of eddies, defined by OK after 10 growth rates at the surface.*

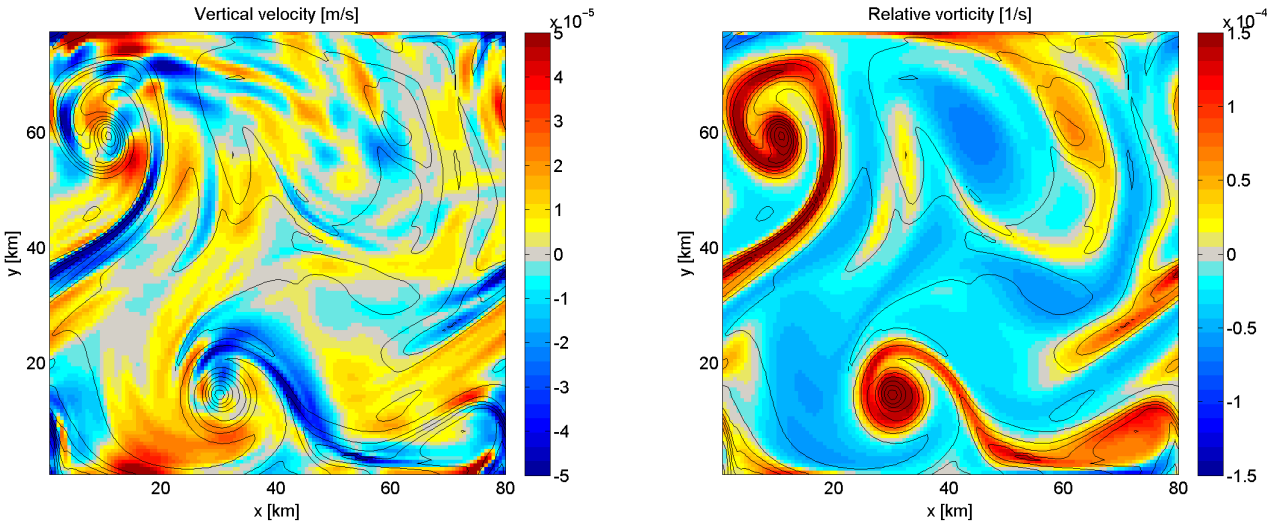

Figure 3.21.: *Vertical velocity with contours of temperature (a) and relative vorticity (b) for a submesoscale lower resolution experiment (exp. 3 in table 2.3) during the turbulent phase of the instability process at the surface*

In figure 3.21 the vertical velocity with overlaying contours of temperature can be seen in (a) and the corresponding vorticity (b) for the lower resolution submesoscale experiment (experiment 3 in table 2.3). Clearly visible are the enhanced vertical velocities associated with the concentrated temperature lines in the spiral structure, while the rest of the domain, associated with anticyclonic vorticity possesses only low values of vertical velocity. From figure 3.21 (b) the asymmetry of high absolute vorticity values can be concluded. The positive maximal values are about 5 times higher than the negative ones and concentrated in the spiral like patterns, while the negative vorticity is distributed more widely over the whole domain.
We noticed that only one type of cyclonic spirals is evolving in the simulation, whereas two different types are imaginable. This is illustrated in figure 3.22.

$$\frac{D\zeta}{Dt} = (f + \zeta)\frac{\partial w}{\partial z} \tag{3.8}$$

With the utilisation of the vertical component of the vorticity equation (3.8 (*Vallis*, 2006)) we can eliminate the both spiral types depicted on the right side of figure 3.22. In *Vallis* (2006) this equation contains an additional term related to the $\beta-$ effect, which we neglected here. In the beginning of an instability process

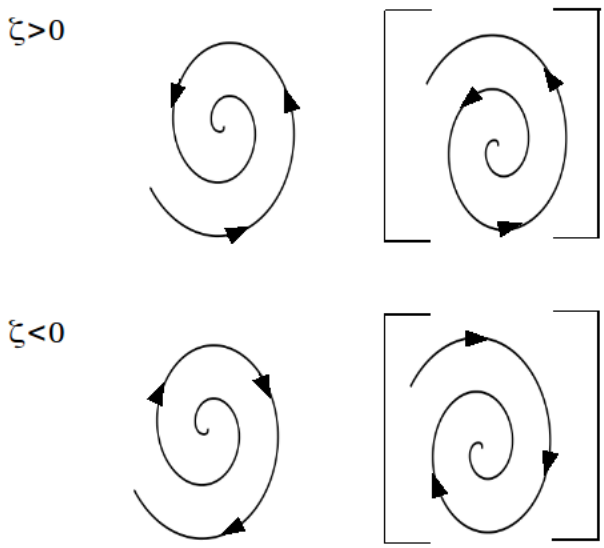

Figure 3.22.: *The upper left schematic represents a convergent cyclonic spiral, the upper right schematic represents a divergent cyclonic spiral, the lower left schematic represents a divergent anticyclonic spiral and the lower right schematic represents a convergent anticyclonic spiral. The upper and lower right spirals do not evolve (for explanation compare equation 3.8).*

we can assume the relative vorticity (ζ) to be small. The Coriolis parameter (f) does not change the sign, thus we can directly relate the relative change of ζ to the sign of the vertical velocity change with depth. In a downwelling region the sign of $\frac{\partial w}{\partial z}$ is positive, which directly leads to an increasing positive relative vorticity ζ. Analogue upwelling regions can be associated with negative vorticity. Divergent cyclonic spirals would lead to upwelling and thus a negative change of ζ, which leads to a decrease of the original positive ζ (convergent anticyclonic spirals would lead to downwelling and thus a positive change of ζ, which leads to a decrease of the original negative ζ). From this we conclude that only cyclonic convergent and anticyclonic divergent spirals are possibly self-energysing and thus evolving.

Figure 3.23 (a), shows OK after 15 growth rates for the mesoscale experiment. No difference in the structure for cyclones and anticyclones is observable (b). Compared to the submesoscale run the relative vorticity is distinctly lower (b). The associated

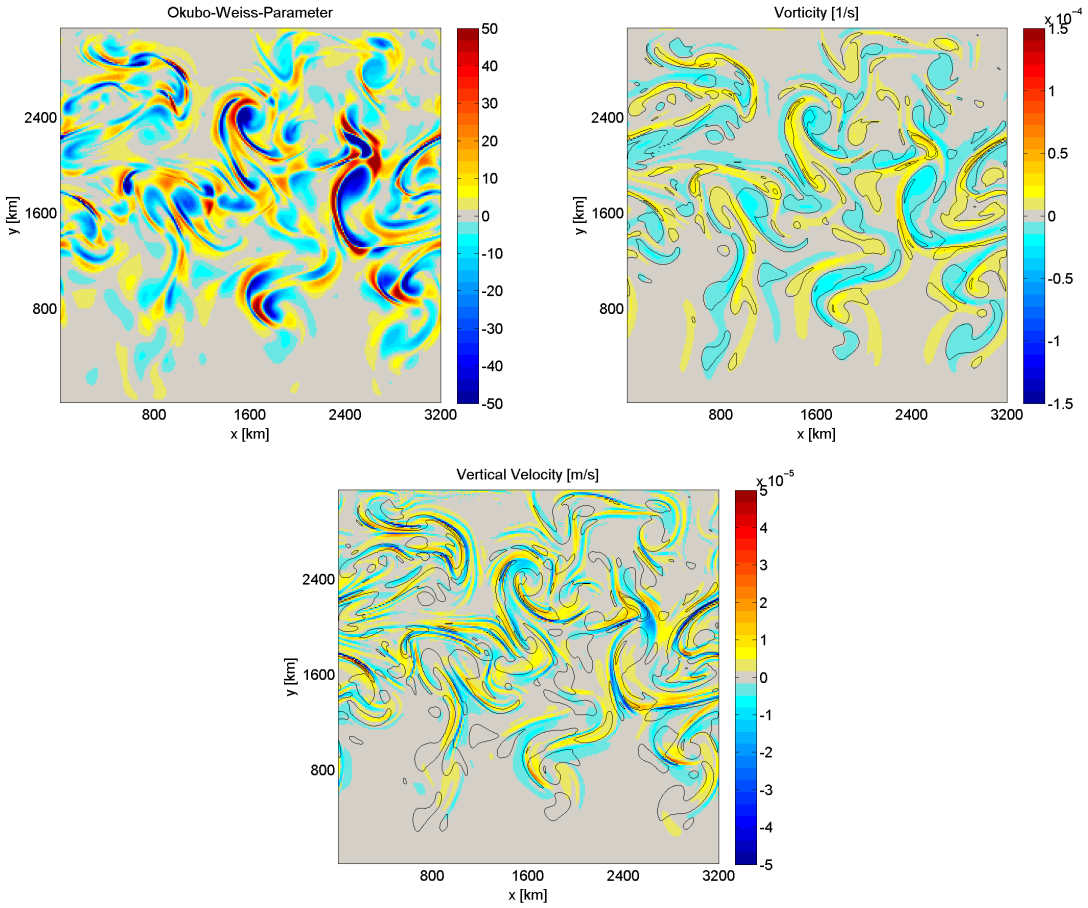

Figure 3.23.: *Mesoscale: OK (a), relative vorticity (b) and vertical velocity (c) with contours of eddies, defined by OK after 15 growth rates at the surface.*

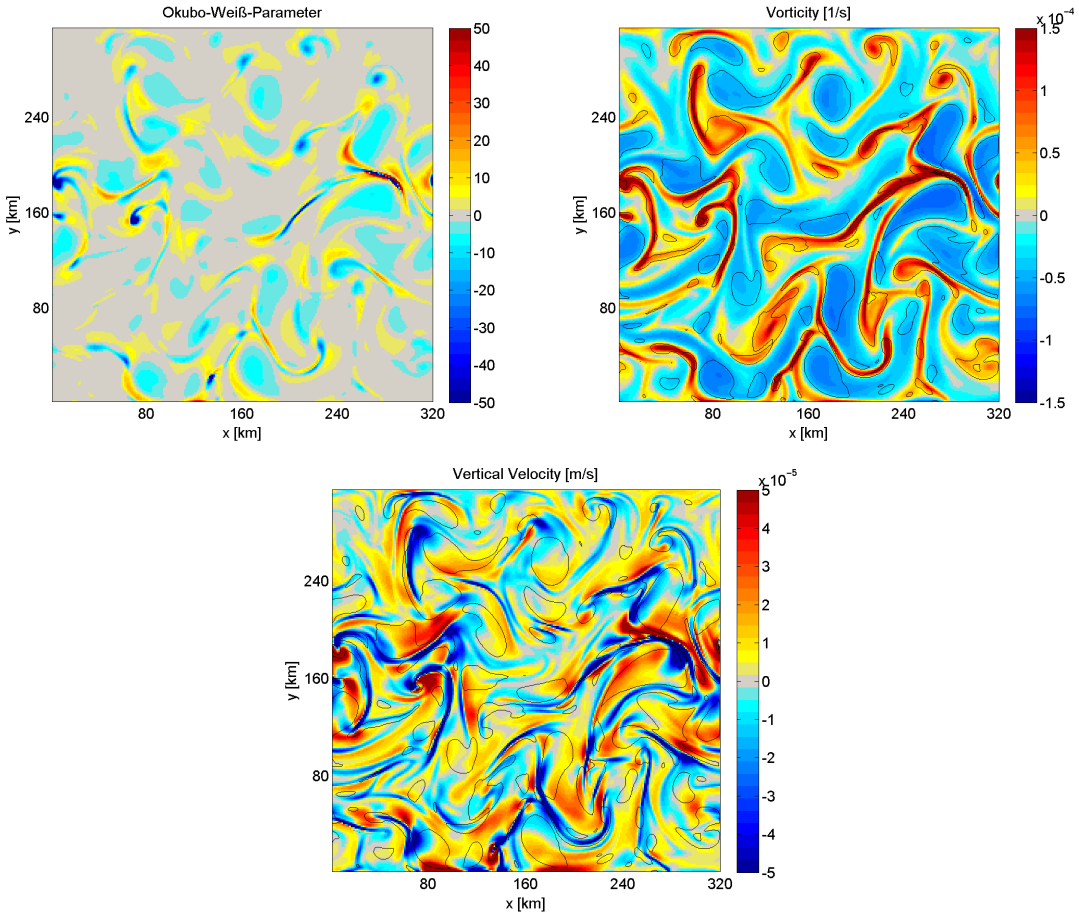

Figure 3.24.: *Intermediate: OK (a), relative vorticity (b) and vertical velocity (c) with contours of eddies, defined by OK after 17 growth rates at the surface.*

vertical velocity is mostly zero at the centre of the eddies and high in the surrounding (compare figure 3.23 (c)). This might be simply due to horizontal gradients or due to some submesoscale activity existent in the mesoscale simulation (which was already seen in the distribution of *Ro*).

The intermediate simulation appears similar to the submesoscale run, but with lower OK values (figure 3.24 (a)). The vorticity is as high as in the submesoscale experiment (b). The cyclonic regions are filamentlike, but not rolled into spirals. Furthermore they are associated with enhanced vertical velocities (c), while the anticyclones have lower vertical velocities.

The OK reveals different structures of the eddies in the submesoscale and the mesoscale regime. Furthermore a clear difference between cyclones and anticyclones becomes observable in the submesoscale dynamics. The cyclones are, at least in the beginning, smaller but more intense, featuring the characteristic spiral like structure. Furthermore cyclones are always associated with enhanced downward vertical velocities, whereas submesoscale anticyclones and mesoscale eddies feature nearly zero vertical velocities in the centre.

In figure 3.25 the surface distribution of *Ro* after 27 growth rates is shown without eddies, without anticyclones and without cyclones, defined by OK for the submesoscale experiment. All regions identified as eddies by OK have been subtracted therefore from the domain, befor calculating the distribution. The remaining values are separeted into cyclones and anticyclones by their vorticity (negative or positive). The distribution is distinct different when subtracting the cyclones, but only a small difference can be seen when substracting the anticyclones. The distribution without all eddies is nearly normal distributed. This confirms again, that more positive extreme high *Ro* exist than negative ones. Furthermore this extreme values are actually associated with the eddy regions.

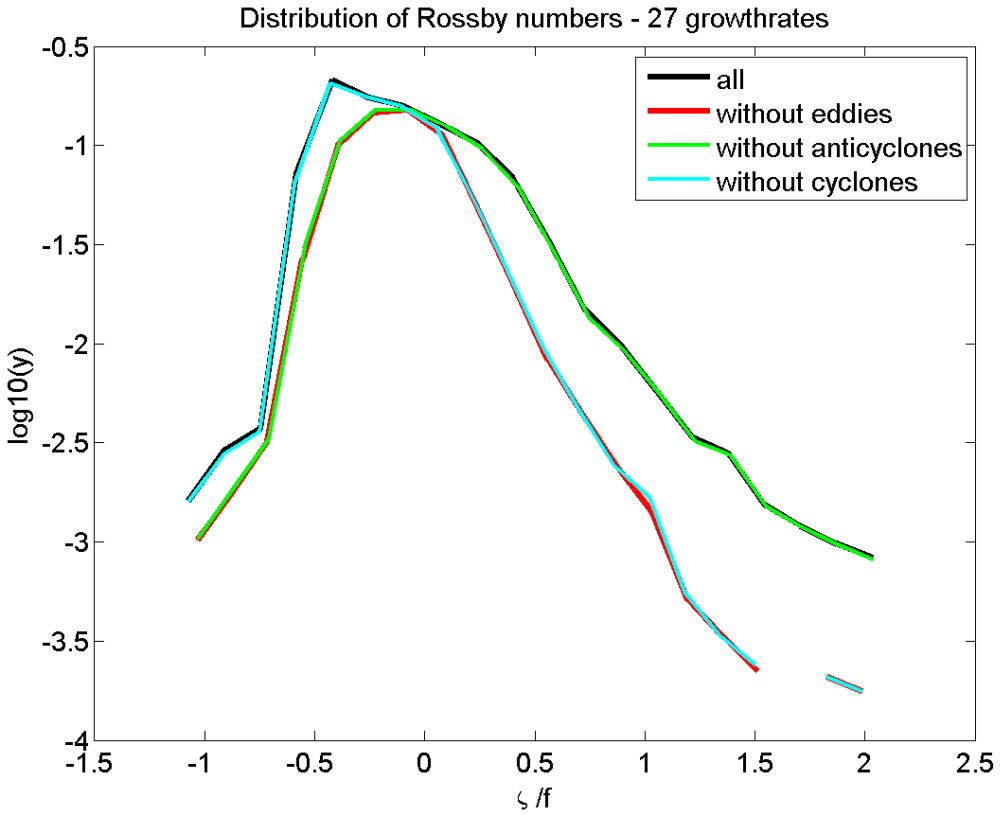

Figure 3.25.: Submesoscale: Distribution of $Ro(\frac{\zeta}{f})$ after 27 growth rates in the surface layer. Without eddies (red), with eddies (black), without cyclones (light blue) and without anticyclones (green). Regions defined as eddies by the OK, are substracted from all values for the red curve. Positive relative vorticity values in this eddy regions define cyclones and negative relative vorticity in an eddy defined by OK represent an anticyclone.

4. Summary and Discussion

4.1. Reproducing baroclinic instabilities in numerical simulations

We were able to reproduce the baroclinic instability process with an idealised box model without topography and without forcing (spin-down experiment) for different dynamical regimes, consistent with observed ones.

The energy development of all simulations is very similar, EKE starts rising when the temperature and velocity field starts meandering, reaches its maximum when the eddies are separating and declines when the eddies become weaker (spin-down experiments). Thereby we can compare the different experiments at characteristic stages of the process.

From the temperature fields we can already recognise distinct differences in the structure of the growing instabilities. In the submesoscale case eddies evolve only as cold perturbations in warmer surrounding, while in the mesoscale regime both, warm and cold eddies are found. The structure of the submesoscale eddies are filaments rolled into a spiral, whereas the mesoscale circulation pattern is more closed and vortex-like. The amplitude of horizontal velocity in the mesoscale simulation exceeds the velocity of the submesoscale run. Vertical structure of buoyancy and horizontal and vertical velocity, as well as length and timescales correspond to the ones predicted by LSA. For submesoscale conditions the fastest growing wavelength found is about 1.9 km, growing to length scales of 10 km at the end of the simulation, correspondent with typical observational data for submesoscale lengths (compare e.g. *Munk et al.* (2000)). The maximal growth rate is 1.34 day^{-1}, which is on the same order of magnitude with growth rates calculated from measurements (e.g. *Boccaletti et al.* (2007)).

In mesoscale ranges, simulation and LSA reveal initial length scales of 75 km, ending up with length scales of 300 km. The associated maximal growth rate of about 0.04 day^{-1} coincide with the interior mode of *Boccaletti et al.* (2007). In the intermediate range the length scales are initially of the order of 7.6 km, growing to sizes of 40 km.

The depth structure of buoyancy and velocity predicted by LSA is similar to the simulated structure in the submesoscale experiment, however it matches not that well, as in lower resolution runs or as in intermediate and mesoscale simulations. One reason could be the early breakdown of symmetry in the submesoscale experiment, even before the perturbation structure predicted by LSA can fully develop. Another reason is that the predicted fastest growing wave length does not fit in the domain, thus a slightly different wave length is growing in the simulation, which might lead to the difference of simulated and predicted depth-structure.

Neither can LSA predict an asymmetry between maximum and minimum perturbations nor is an asymmetry visible during the linear phase in the simulated ones. However we are not able to eliminate the possibility that a already in the beginning of the instability process a qualitative difference between cyclones and anticyclones exists.

Additionally to the predicted dominant wavenumber a second peak in wavenumber space is observable for all three regimes. This could be either a subharmonic of the dominant wave or the ageostrophic mode described by *Stone* (1970).

4.2. Verifying cyclonic dominance in submesoscale dynamics

The developement of the dimensionless numbers Ro and Ri over time show that all experiments represent the predefined dynamics. Nevertheless, when the process comes in the decaying phase the submeso- and intermediate scale experiments reaches Ro, Ri and length scales typical for mesoscale dynamics. The mean Ro and also the fraction of gridpoints above (below) submesoscale Ro (Ri) are very similar

for the submesoscale and the intermediate regime, while they are distinctly lower in the mesoscale regime. However in the submesoscale experiment higher extreme values are found in the distribution of Ro and the surface snap shots of vorticity. Locally maximal values of $Ro = 5$ are found, while the intermediate Ro does not exceed values of two, whereas mesoscale Ro stay below one.

The mean positive Ro features higher values than the negative mean in submesoscale and intermediate regimes, whereas positive and negative mean are equal in the mesoscale simulation. The standard deviation of positive Ro in the submesoscale and the intermediate regime represents higher extreme values of positive Ro (associated with cyclonic circulation). In the intermediate and submesoscale ranges a surface intensification of extrem high values of Ro can be found, while in the mesoscale regime high values occur at the bottom and the surface. All three regimes have a positive skewed distribution of Ro, although the submesoscale skewness exceeds the mesoscale one by about a factor of three. The initial zero values of the skewness in all three regimes indicate, that no dominance of cyclones exists in the beginning.

The enhanced dominance of cyclonic motion in submesoscale dynamics is confirmed hereby and the simulations are thus suitable for further investigations concerning structural and spatial differences between cyclones and anticyclones.

4.3. Different force balances in mesoscale and submesoscale dynamics

The ageostrophic velocity component features the same order of magnitude in all dynamical regimes, though in relation to the geostrophic velocity component, it is significantly higher for submesoscale conditions. This was quantified with a maximal value of the relation between ageostrophic and geostrophic KE of 0.15 in the submesoscale experiment, while the mesoscale relation does not exceed 0.005. This represents the importance of ageostrophic flow components in the submesoscale dynamics, while it is neglictable in the mesoscale regime. Nevertheless the ageostrophic

KE never exceeds the geostrophic one, and is thus not dominating. Furthermore the structure of ageostrophic and geostrophic flow components was considered. In the submesoscale and the intermediate regime high ageostrophic values can be always associated with eddy regions. The ageostrophic velocity is anticyclonic in cyclonic regions, as also seen in the simulation of *Eldevik and Dysthe* (2002). This might be due to friction, which acts always against the total velocity, but further investigations would be necessary to figure the dependence of the ageostrophic relative vorticity on the ageostrophic terms (friction, tendency and advection).
In contrast the mesoscale structure of high ageostrophic velocities cannot directly be connected with the eddy regions or a dominant rotational direction.
The higher importance of ageostrophic flow components in the submesoscale regime was confirmed, as well as the different size of the evolving negative and positive pressure perturbations.

4.4. Enhanced vertical velocities and spiral structures in submesoscale dynamics

To confirm the enhanced vertical velocities, which we assume to be responsible for the strutural differences between cyclones and anticyclones in the submesoscale range, the Okubo-Weiss-parameter (OK) was introduced to identify eddy regions. The analysis of the eddies defined by OK and the associated structures of vorticity, pressure perturbation and vertical velocity reveal, yet another time, distinct differences in the structure of eddies in the submesoscale and the mesoscale regime. In the initial phase the structure of cyclonic eddies is filament-like for intermediate and submesoscale simulations, while it is vortex-like in the mesoscale regime for cyclones as well as for anticyclones. The submesoscale anticyclones are clearly larger, but with lower absolute values of relative vorticity. Later on, the filaments are rolled into spirals in the submesoscale experiments. The relative vorticity is about one order of magnitude lower for the mesoscale experiment, compared to the submesoscale and

the intermediate simulation. The vertical velocity is mainly zero in the center of all mesoscale eddies and low in submesoscale and intermediate anticyclones, while enhanced vertical velocities occur in submesoscale cyclones. There the vertical velocity is directed mainly downward, i.e. the spirals are associated with a convergent flow field. In all regimes the amplitude of positive and negative pressure anomalies is of the same magnitude, but the size of low pressure systems is smaller than the size of high pressure systems in the submesoscale and the intermediate simulation.

During the time of this thesis we performed a number of differnet simulations for submesoscale and mesoscale regimes. We started with lower resolution simulations and simulated experiments with slightly different initial conditions, furthermore several simulations had to be repeated, due to computational problems and restarting of the servers. All simulations revealed similar results to the presented ones. Although the depicted results are not that representative as a statistical ensemble would be, we think that our findings are no result of coincidence. However, to generalise the main results of this thesis it would be convenient to analyse a statistical ensemble of different simulations with same initial conditions.

4.5. Conclusion

The reported structural differences of vertical velocity, relative vorticity and pressure anomaly for meso- and submesoscale dynamics, utilising the theory of cyclostrophic balance (1.3) and the classification of velocity singularities in the divergence-vorticity parameter space defined by *Okubo* (1970) and already mentioned in section 1.3 support our initial presented hypothesis.
In the mesoscale regime the geostrophic balance between pressure gradient force and the Coriolis force leads to equal sized cyclones and anticyclones. Assuming equal pressure perturbations (and the same Coriolis force) in the beginning, pressure force and Coriolis force are balancing each other, resulting in equal velocitiy amplitudes in low and high pressure systems, but in opposed directions. This is contrary to the

submesoscale regime where the centrifugal force has to be taken into account, which is always directed outward.

In a high pressure system the centrifugal force acts in the opposite direction as the Coriolis force, leaving for the pressure force only to balance the difference between the Coriolis force and the centrifugal force. In a low pressure system the centrifugal force is also directed outward but in opposite direction as the pressure force. In this case the pressure force has to balance both, the Coriolis and the centrifugal force.

When still assuming equal pressure and velocity perturbations in the beginning of the instability process (which is given in our simulation, as could be seen from the along-stream-sections of perturbation velocity and buoyancy, as well as from the surface pressure anomalies in section 3.3.2) this leads to smaller length scales for low pressure systems (cyclones). With equal pressure amplitudes the resulting pressure gradient is higher, for smaller length scales, resulting in a higher pressure force. This argument is well known from literature (e.g *Cushman-Roisin and Beckers* (2011)) and observations, mainly from Meteorology (e.g. (*Klein*, 1958)), but has not been applied to the cyclone-anticyclone asymetry of spiral eddies so far. The presented results are in accordance with this theory. The cyclones found in the submesoscale simulation were smaller in size, with enhanced pressure and velocity gradients. We further found, that the enhanced horizontal gradients in cyclonic eddy regions, are associated with enhanced vertical velocities (figure 3.20 (b) and 3.21).

This leads us now to the structural differences of divergent and non-divergent flow fields. As shown in section 1.3, spiral structures of eddies are only possible when the velocity field is divergent. In non-divergent velocity fields only closed circulation patterns (called vortices) can evolve. It is well known that the mesoscale regime is assumed to be 2-dimensional, with negligible vertical velocities, contrary to the submesoscale regime, which is associated with enhanced vertical velocities.

Divergence and vertical velocities are associated parameters, i.e. in a non divergent velocity field we have negligible vertical velocities, while divergence and convergence lead to enhanced vertical velocities. The spiral structures occur only in divergent or convergent velocity fields, thus they occur with enhanced vertical velocities.

Now the known arguments of gradient-wind-balance and the structure of vortices in divergent and non-divergent flow fields can be connected. The force balance in submesoscale regimes leads to smaller cyclones. This also implies that horizontal gradients of velocity and pressure are sharpened in cyclonic regions. Therefore enhanced vertical velocities are associated with submesoscale cyclones. Enhanced vertical velocities imply a non-divergent flow field and only in non-divergent flow fields spiral structures of eddies can evolve. Some spiral pattern might be visible in the mesoscale simulation because at the edge of mesoscale activity also submesoscale variability manifests (which was for example seen in the distribution of Ro, where in some few points Ro approaches values of one, implying by definition submesoscale dynamics). Furthermore the two-dimensionality of the mesoscale regime is only an assumption, whereas effectively also in mesoscale dynamics low values of vertical velocity occur.

A. Appendix

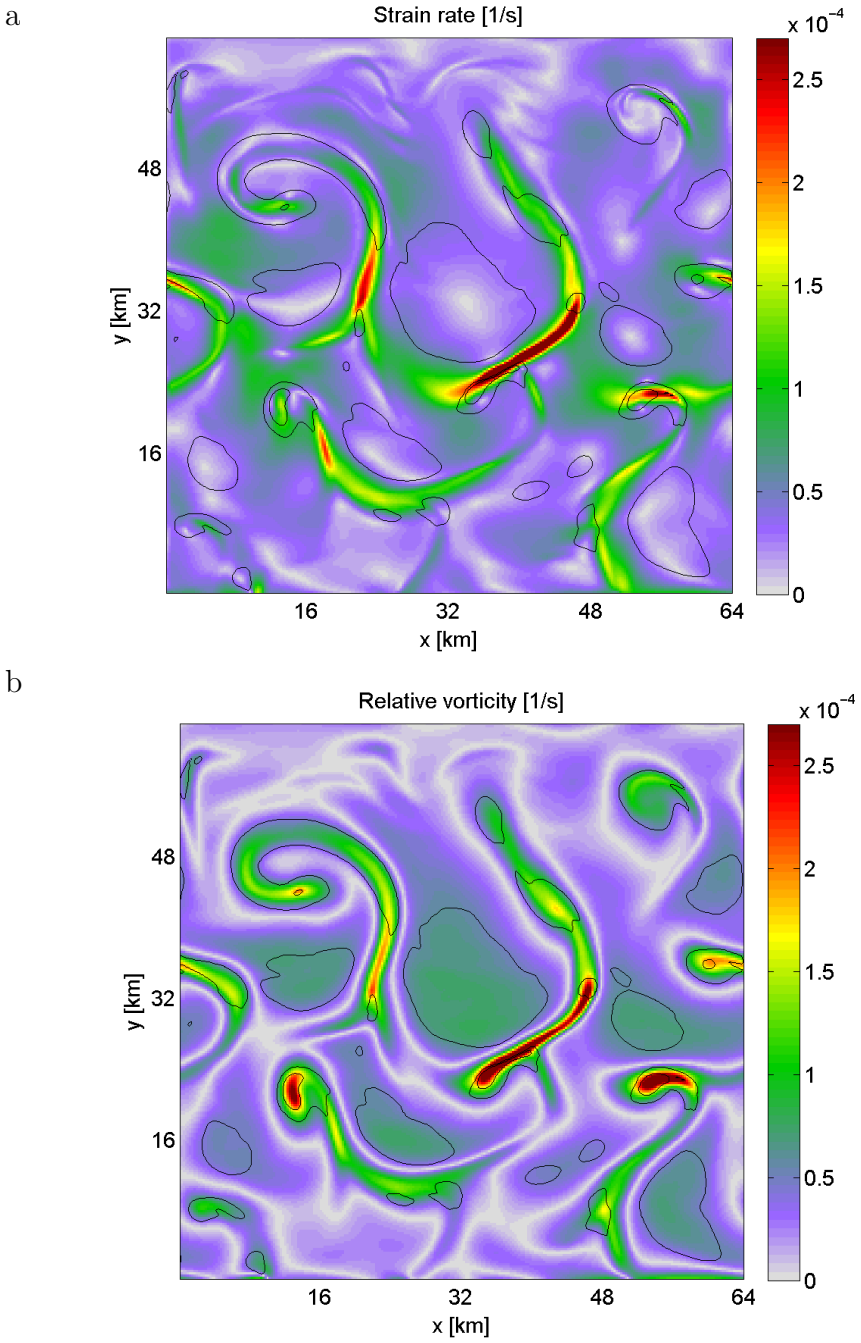

Figure A.1.: *Submesoscale: (a) Strain rate as defined in section 3.3.3 and (b) relative vorticity at the surface, during the turbulent phase. Contours show the Okubo-Weiss-parameter.*

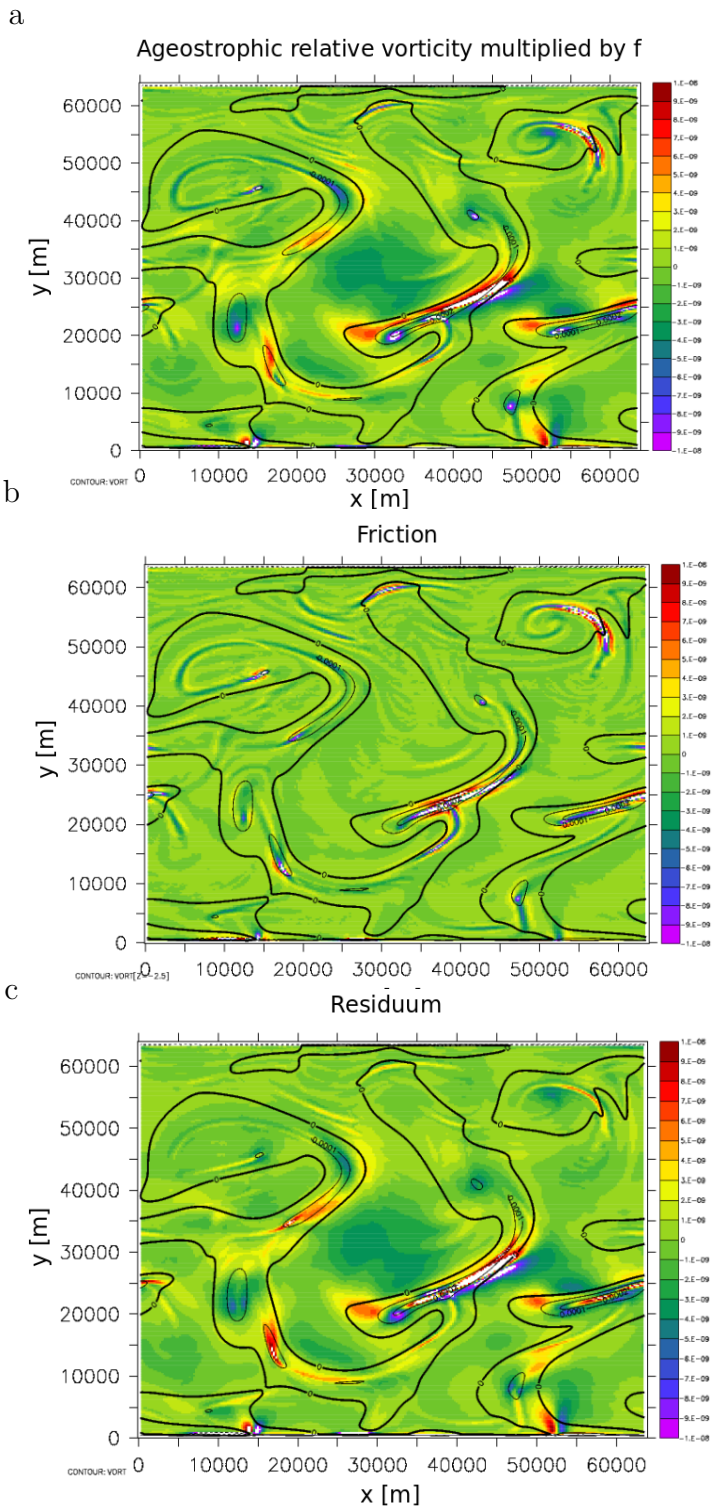

Figure A.2.: *Submesoscale: (a) Coriolis term in equation 3.5 (relative ageostrophic vorticity, multiplied by f) , (b) friction term in equation 3.5 and (c) the residuum (advection and tendency terms in equation 3.5) All figures are surface plots during the turbulent phase of the instability process.*

B. Acknowledgment

First I would like to thank Prof. Dr. Carsten Eden for the supervision of my work and continuous support during my Master studies, for providing the model pyOM, as well as the derivation and the numerical code of the linear stability analysis.
Special thanks go to Nils Brüggemann for supervising my thesis, for helping me answering a lot of questions, for all the motivation and discussions about my work and the correction of this thesis.
I also want to thank Prof. Dr. Detlef Stammer for reviewing this thesis.
Furthermore I would like to thank Prof. Dr. Gualtiero Badin for helpfull suggestions and comments on my thesis.
I thank Julius Lensch, Lukas Vollmer and Daniel Hirschmeier for proofreading the text.

Bibliography

Badin, G., A. Tandon, and A. Mahadevan (2011), Lateral mixing in the pycnocline by baroclinic mixed layer eddies, *Journal of Physical Oceanography*, *41*(11), 2080–2101.

Boccaletti, G., R. Ferrari, and B. Fox-Kemper (2007), Mixed layer instabilities and restratification, *Journal of Physical Oceanography*, *37*(9), 2228–2250.

Brüggemann, N., and C. Eden (2012), A closure for meso- and submesoscale processes in the upper ocean mixed layer, in preparation.

Capet, X., J. McWilliams, M. Molemaker, and A. Shchepetkin (2008), Mesoscale to submesoscale transition in the california current system. part ii: Frontal processes, *Journal of Physical Oceanography*, *38*(1), 44–64.

Cho, J., and L. Polvani (1996), The emergence of jets and vortices in freely evolving, shallow-water turbulence on a sphere, *Physics of Fluids*, *8*(6), 1531–1552.

Cushman-Roisin, B., and J. Beckers (2011), *Introduction to geophysical fluid dynamics: Physical and numerical aspects*, Academic Press.

Dokken, S., and T. Wahl (1996), Observations of spiral eddies along the norwegian coast in ers sar images, *Tech. rep.*

Eady, E. (1949), Long waves and cyclone waves, *Tellus*, *1*(3), 33–52.

Eden, C. (2011), A closure for meso-scale eddy fluxes based on linear instability theory, *Ocean Modelling*, *39*(3), 362–369.

Eldevik, T., and K. Dysthe (2002), Spiral eddies, *Journal of Physical Oceanography*, *32*, 851–869.

Emelianov, M., C. Millot, and I. Taupier-Letage (2004), Spatial structure of anticyclonic eddies in the algerian basin (mediterranean sea) analyzed using the okubo–weiss parameter, *Deep-Sea Research*, *2*(51), 3009–3028.

Haine, T., and J. Marshall (1998), Gravitational, symmetric, and baroclinic instability of the ocean mixed layer, *Journal of Physical Oceanography*, *28*, 634–658.

Hakim, G., C. Snyder, and D. Murakil (2002), A new surface model for cyclone-anticyclone asymmetry, *Journal of the atmospheric sciences*, *59*(16), 2405–2420.

Hoskins, B., and F. Bretherton (1972), Atmosphere frontogenesis models: mathematical formulation and solution, *J. atmos. Sci*, *29*, 11–37.

Klein, W. (1958), The frequency of cyclones and anticyclones in relation to the mean circulation., *Journal of Atmospheric Sciences*, *15*, 98–102.

Koszalka, I., A. Bracco, J. McWilliams, and A. Provenzale (2009), Dynamics of wind-forced coherent anticyclones in the open ocean, *J. Geophys. Res*, *114*, C08,011.

Molemaker, M., J. McWilliams, and I. Yavneh (2005), Baroclinic instability and loss of balance, *Journal of physical oceanography*, *35*(9), 1505–1517.

Munk, W., L. Armi, K. Fischer, and F. Zachariasen (2000), Spirals on the sea, *Proceedings of the Royal Society of London. Series A: Mathematical, Physical and Engineering Sciences*, *456*(1997), 1217.

Okubo, A. (1970), Horizontal dispersion of floatable particles in the vicinity of velocity singularities such as convergences, *17*(3), 445–454.

Olbers, D., J. Willebrand, and C. Eden (2012), *Ocean Dynamics*, Springer Verlag Berlin.

Roullet, G., and P. Klein (2010), Cyclone-anticyclone asymmetry in geophysical turbulence, *Physical review letters*, *104*(21), 218,501.

Scully-Power, P. (1986), Navy oceanographer shuttle observations, sts 41-g mission report, *Tech. rep.*, DTIC Document.

Skyllingstad, E., and R. Samelson (2012), Baroclinic frontal instabilities and turbulent mixing in the surface boundary layer. part i: Unforced simulations, *Journal of Physical Oceanography*, (2012).

Stone, P. (1966), On non-geostrophic baroclinic stability, *Journal of the Atmospheric Sciences*, *23*(4), 390–400.

Stone, P. (1970), On non-geostrophic baroclinic stability: Part 2., *Journal of the Atmospheric Sciences*, *27*(4), 721–726.

Stuart, J. (1967), On finite amplitude oscillations in laminar mixing layers, *J. Fluid Mech*, *29*(part 3), 417–440.

Thomas, L., A. Tandon, and A. Mahadevan (2008), Submesoscale processes and dynamics, *Eddy resolving ocean models, Geophysical Monograph*, *177*, 17–38.

Vallis, G. (2006), Atmospheric and ocean fluid dynamics: Fundamentals and large-scale circulation.

Statutory Declaration

I hereby declare that the thesis has been written by myself without any external unauthorised help, that it has been neither presented to any institution for evaluation nor previously published in its entirety or in parts. All quotations, figures and ideas which are quoted from or based on other sources have been marked as such without exception. I agree that a version of this thesis may be made available in the Library of the University of Hamburg.

Hannah Kleppin, Hamburg 6th November